UNIVERSITÀ DEGLI STUDI DI PALERMO
Information And Communication Technologies
ING-INF/03-Telecomunicazioni
Dipartimento di Ingegneria

Robust Communications for the Underwater Internet of Things

Ph.D. Candidate
Ing. CONCETTA BALDONE

Coordinator
Prof. ILENIA TINNIRELLO

Tutor
Prof. ILENIA TINNIRELLO

Co-Tutors
Prof. CHIARA PETRIOLI
Prof. DANIELE CROCE
Prof. STEFANO MANGIONE

XXXIV CYCLE - ACADEMIC YEAR 2022-2023

Abstract

In recent years, the emergence of numerous applications and activities involving the underwater world have given rise to a new class of technologies that takes the name of Internet of Underwater Things (IoUT). Submarine activities such as remote control, pollution monitoring, data collection, disaster detection or even early warning and assisted navigation are just some of the main applications that require the use of underwater communication systems capable of providing connectivity between static and mobile nodes deployed at different depths. Generally, underwater communications employ audio signals which can propagate relatively far but are also significantly affected by Doppler distortions. In fact, physical properties of the water and spatial changes due to tides, currents and waves can cause channel variations or unwanted movements of the transmitter or receiver. A plethora of underwater communication techniques have been developed to address such challenging scenarios. In this thesis, we study how to correct Doppler effects in transmission employing JANUS, the first standard for underwater acoustic communication. In particular, we exploit the JANUS preamble, composed of an m-sequence of 32 pseudo-random symbols, to estimate and compensate for the Doppler shift caused by the relative motion of transceivers up to 5 m/s. The proposed method is validated using Watermark simulator and at-sea experiments. Then, we analyze the performance of S2C both in simulation and in- field experiments, based on our own S2C implementation. We undertake extensive simulation experiments, quantitatively measuring the impact of a variety of modulation parameters (such as the sweep duration and the number of coded symbols per sweep), and under different channel characteristics (depth, range, Doppler speed, etc.). Furthermore, we test the performances of the S2C modulation at sea, obtaining good results also in shallow waters.

Contents

List of Figures

List of Tables

Chapter 1

Introduction

In recent years, the emergence of numerous applications and activities involving the underwater world have given rise to a new class of technologies that takes the name of Internet of Underwater Things (IoUT). Submarine activities such as remote control, pollution monitoring, data collection, disaster detection or even early warning and assisted navigation are just some of the main applications that are of interest not only for scientific research but also for the industry and marine defense [1]. While each of these applications has different purposes, they all require underwater communication systems that are capable of providing connectivity between static and mobile nodes deployed at different depths to perform cooperative monitoring, operations and data collection tasks. A typical underwater application consists of several underwater sensors that are placed on the sea floor or anchored to floating buoys and used to sense various environmental information such as water quality, temperature, pressure, chemical and biological elements, and so on. For example, to perform real-time monitoring of the environment, the sensors need an underwater network that allows to transmit collected data from the underwater environment to the mainland and without employing long cables or an operator who dives to collect data manually. Other applications can instead involve autonomous underwater vehicles (AUV) or autonomous surface vehicles (ASV) to explore the underwater world or to support a submarine in distress [2]. In both cases, a wireless communication is a desirable condition to allow maximum freedom of maneuver for vehicles.

However, differently from what happens for terrestrial IoT, common Radio Fre-

quency (RF) technologies do not work well in underwater conditions due to the extreme attenuation of the medium. Indeed, although transmissions of information can be carried out by means of acoustic, electromagnetic (EM) or optical waves, most of today's underwater communication systems make use of sound waves which have the advantage of significantly less absorption at low frequencies (around a dozen kHz) compared to the radio and optical communications. Acoustic communication enables longer coverage distances while maintaining a low bitrate (dozens of kbps). However, due to frequency selectivity, multipath, and significant Doppler effects, underwater acoustic channels are a significant bottleneck in marine data networks. The data rates are constrained by significant delay spreads and path-dependent Doppler shifts: when sound travels through multiple paths, the delay spread is on the order of tens or hundreds of milliseconds, and fluctuations result in path-dependent Doppler shifts that are not uniform across the acoustic signal's spectrum. Due to the low speed of about 1500 m/s (i.e. five orders of magnitude less than the speed of electromagnetic waves) with which sound waves propagate in water, Doppler effects can be very severe. Furthermore, the presence of Doppler distortion can be considered an ubiquitous condition in these environments, since,in addition to deliberate node's movements, also tides, currents and waves can cause unintentional transmitter/receiver motion (drifting) in some cases at comparable velocities of mobile nodes [3]. For all these reasons, measuring and compensating Doppler effects is an essential requirement to create a robust and reliable underwater acoustic communication system. Another important feature that distinguishes underwater acoustic communications is the large variety of environments and scenarios that can be presented.Each of these can vary in terms of depth, temperature, noise, density of fauna or even geological structure. All these factors influence acoustic propagation structure, multipath magnitude, delay and Doppler spread, etc.

To cope with all this variety of conditions, a plethora of acoustic underwater modems have been developed to meet the needs of different conditions and applications. Some of these are based on coherent modulations [4] or on multicarrier modulations (such as OFDM) which are characterized by a high spectral efficiency and therefore by a high bit rate (with nominal data rates of hundreds of kbit/s).However, the latter can be used for short/medium distance transmissions (from tens to hundreds of meters) and are very sensitive to Doppler and delayed diffusion. In this

case, appropriate and complex channel and Doppler estimates and compensations must be applied and updated frequently throughout the transmission. Furthermore, it has been found that in some very harsh underwater environments, applying a modulation scheme such as OFDM may not be feasible at all[5]. In such harsh environments, a different class of modulation scheme can ensure connectivity although with low spectral efficiency. This category of modulation schemes includes spread spectrum modulations such as those based on frequency hopping or those based on chirp signals, which have the characteristic of being particularly robust even in the presence of Doppler spread, selective multipath, etc. Because of its robustness and reliability, this type of modulation is used in acoustic modems, either individually for all applications where data delivery is more important than speed of reception or as fall-back modulations to ensure connection continuity (even at a lower bit rate) when high bit rate modulations cannot be used due to temporary and adverse channel conditions.

In this thesis, we propose a Doppler estimation algorithms based on the Cross Ambiguity Function method (CAF) that can be used in real-time applications to estimate and compensate Doppler distortions in underwater acoustic communications that use the JANUS standard [6]. The latter is the first standard for underwater acoustic communications developed and established in March 2017 by the NATO Center for Maritime Research and Experimentation (CMRE) to overcome the lack of interoperability between different assets and devices marketed up to now by different manufacturers and based on several proprietary modulation schemes. The modulation scheme adopted by JANUS consists in a Frequency-Hopped Binary Frequency Shift Keying (FH-BFSK) and we exploit the JANUS preamble, composed of an m-sequence of 32 pseudorandom symbols, to compensate for doppler distortions without requiring any modification to the standard. We validate the proposed method using Watermark [7], a realistic underwater channel simulator, and with in field extensive experimental campaign in the LOON (Littoral Ocean Observatory Network) test bed, located in the Harbor of La Spezia in Italy and developed by CMRE. As we will show, our estimation technique is able to correct and receive over 90% of the packets even with severe Doppler caused by relative movements of the transceivers up to 5 m/s. Another contribution of this thesis work concerns the sweep-spread carrier (S2C) modulation, an innovative communication method

based on a non-conventional carrier signal used to convey modulated data through the underwater channel. The sweep-spread carrier method has been presented by Kebkal et al. in [8] as a robust and reliable communication method for transmitting acoustic signals in underwater communication channels commonly affected by severe multipath and Doppler effects. Underwater modems based on S2C modulations and with a nominal bit rate of 13.9 kbps have been patented and successfully adopted in real-world deployments. In this thesis work, we analyze the performance of S2C both in simulation and in field experiments, using a custom S2C software implementation. We undertake extensive simulation experiments, quantitatively measuring the impact of both a variety of modulation parameters, such as the sweep duration and the number of coded symbols per sweep, and several environment characteristics among which bottom depth, transceivers' depth and distance, etc. Moreover, we analyze the impact of severe Doppler distortions caused by relative motions of the transceivers up to ± 5 m/s in different directions (0°, 90°, 45°). Finally, we test the performance of our S2C modulation at sea, obtaining good results in shallow waters.

The rest of the thesis is organized as follows.

In Chapter 2 we give an overview of the main phenomena that characterize underwater acoustic communications such as the Doppler effect, multipath, attenuation, etc. For each of them, we provide a brief description of these phenomena in order to provide the reader with the basic concepts which will then be taken up within the other topics covered by the thesis.

In Chapter 3 we briefly describe two of the robust modulation schemes used in the field of underwater acoustic communication. We describe the JANUS standard by providing its main features such as modulation scheme and packet structure which are of interest for this work. In the same way, we briefly introduce the sweep-carrier method by providing some background knowledge and related works.

In Chapter 4 we give a brief overview of the experimental and simulation platforms used in this work. As simulation platform, we used Bellhop, a ray tracing software for modeling acoustic propagation in underwater environments, and Watermark, a realistic underwater channel simulator for physical-layer algorithms that allows to perform simulations in realistic and reproducible conditions. As experimental platform, we describe the 2020/2021 version of the test bed LOON (Littoral

Ocean Observatory Network) implemented by the NATO STO Center for Maritime Research and Experimentation (CMRE) in the Gulf of La Spezia (Italy), where we conducted several experiments.

In Chapter 5 After a brief review of the Doppler estimation and compensation algorithm present in the literature, we present our estimation technique for underwater acoustic JANUS communication. Then we demonstrate the effectiveness of the proposed method by showing the results obtained both in simulations and real experiments. Simulations were performed by using the realistic underwater channel simulator, while real and extensive experiments were conducted at sea in the Gulf of La Spezia in Italy.

In Chapter 6 we first present our S2C implementation and then analyze the performance of S2C both in simulation and in field experiments by quantitatively measuring the impact of a variety of modulation parameters, such as the sweep duration and the number of coded symbols per sweep, and several environment characteristics.

Chapter 2

Underwater acoustic channel

In this chapter, we describe the submarine acoustic channel. The main features of underwater acoustic propagation are introduced, highlighting in particular the problems related to the characterization of the channel. Acoustic waves are used for data transmission in water because they are the only ones that can propagate over distances greater than 100 m [9]. In fact, both radio waves and optical waves are attenuated over much shorter distances due to the physical properties of the propagating medium. However, the implementation of underwater communication technologies presents several challenges for engineers and scientists in the field. Indeed, acoustic waves propagate more slowly in water than radio waves in air, thus introducing long propagation delays in communications. In addition, the frequencies used are on the order of a few tens of kHz, thus limiting transmission speed. These and other limiting aspects for underwater acoustic communications are described and studied in this chapter.

2.1 Channel characteristics

The propagation of sound in water is governed by complex laws. The description of this phenomenon must take into account many factors, due to the structure of the medium in which it occurs and the boundary conditions represented by the bottom and surface of the water. Underwater propagation of acoustic waves is characterized by the following limiting aspects for communications:

- Dependence on the environmental scenario,
- Multipath components in the channel impulse response,
- Doppler effect,
- Time variance of the impulsive channel response,
- High propagation delays,
- Frequency- and distance-dependent attenuation,
- colored noise.

2.1.1 Environmental scenario

Analyzing experimental data collected in different scenarios, it is evident that there is no typical underwater channel. Precisely, the different characteristics of the channel impulse response are highly dependent on the physical environment in which the devices are placed. A specific geographic area thus determines the typical physical conditions of water, such as temperature, salinity and density, while the instantaneous weather conditions, such as wind speed and direction, determine the presence or absence of surface and internal waves.

In addition, the scenario can be characterized by a deep or shallow seabed. In fact, the characteristics of the medium that dominate propagation are different in the two cases. Particularly in deep bottoms, the profile of the speed of sound depends strongly on the thermocline and the depth of the water. Knowing such a profile, it is possible to derive through mathematical models how sound is instantaneously distributed in three-dimensional space. Using such models, it is also possible to determine in which areas the acoustic wave does not propagate, due to the refractive effect of the sound velocity profile. In contrast, in shallow bottoms, the water creates a waveguide effect in which the acoustic wave reaches all points in the surrounding space, with attenuations that depend on other factors such as the type of bottom. The scenario is also defined by surrounding biological activity, such as presence of microorganisms and other animals that may somehow interfere with acoustic communications. All of these aspects compose a specific scenario that interferes

with the acoustic communication channel. Note that these scenarios depend not only on the geographic area but also on instantaneous conditions.

2.1.2 Multipath

The acoustic waveform that is measured at the receiver, is not only given by the transmitted waveform rescaled by an attenuation coefficient, as is usually the case in the ideal case, but rather results from the superposition of delayed replicas of the transmitted waveform. This phenomenon is represented by multipath delay and caused by the different (resolvable) timings with which the acoustic waves reach the receiver. These arrival times are an effect of propagation occurring along different paths in the water and the distance between the transmitter and receiver. The arrival times and amplitudes of the different paths are strongly dependent on the type and morphology of the seafloor and surface conditions. Therefore, delayed waves arrive at the receiver after the arrival of the direct path (if it exists). This leads to a highly distorted signal and has a negative impact on communication performance.

2.1.3 Doppler effect

The Doppler effect consists of the frequency shift of the carrier due to relative motion between the receiver and transmitter or surface waves and sea currents.

Consider the case of a source that emits a sine wave at frequency f_T while moving at constant speed v towards a fixed receiver as illustrated in figure 2.1. The Doppler effect will alter the wavelength perceived by the receiver: the sine wavelength as seen by the receiver will be decreased by the space covered by the source in a period or, in terms of frequency, the receiver will observe a greater number of wave fronts in the unit of time, i.e. the received frequency f_R will be greater than the transmitted frequency. If by convention we use a positive velocity v to indicate the direction of an approaching source and a negative velocity $-v$ to indicate the direction of a departing source, then we can express the frequency perceived by the receiver as $f_R = \gamma f_T$, where:

$$\gamma = \frac{c}{c - v} \tag{2.1}$$

and c is the speed of sound in water, approximately equal to 1540 m/s.

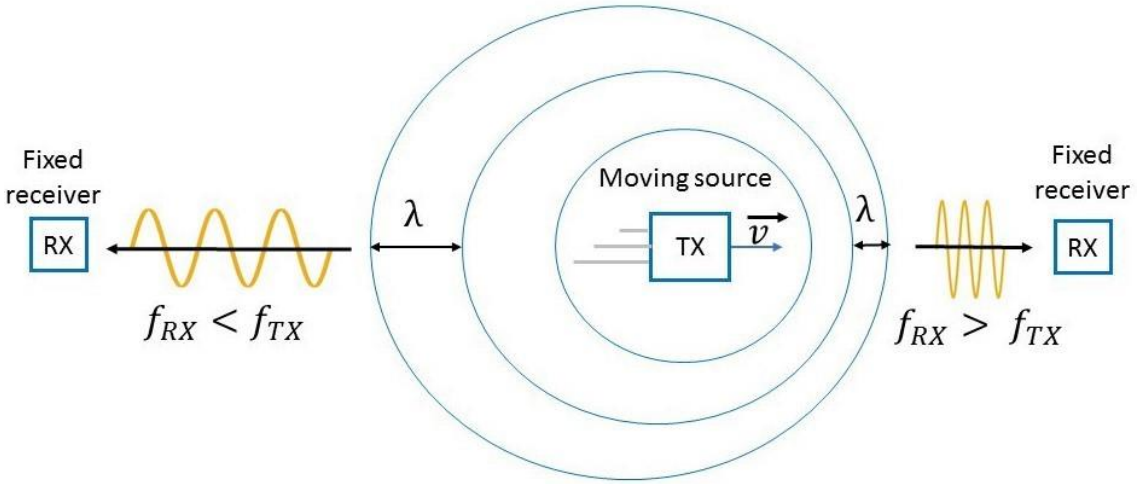

Figure 2.1: Representation of the Doppler effect.

Now, depending on whether the transmitted signal can be considered narrowband or broadband, the Doppler effect has to be modeled differently. For narrowband signals, the Doppler effect can be treated as a simple frequency shift of the whole signal spectrum (i.e. each component is shifted by the same amount of the carrier frequency shift). Instead, for wideband signals, Doppler effect influences differently each frequency component, so the effect is more accurately modeled as expansion or compression of the signal waveform, characterized by a time scaling factor.

2.1.4 Time variance of impulse response

A system is called time variant (TV) if a time shift of the input does not result in the same time shift of the output. In a linear system, this is equivalent to an impulse response $h(t, \tau)$ which is dependent on the instant of observation t, as well as on the delay τ:

$$y(t) = \int_{-\infty}^{\infty} h(t, \tau)x(t - \tau)d\tau \neq \int_{-\infty}^{\infty} h(\tau)x(t - \tau)d\tau \tag{2.2}$$

where $x(t)$ is the system input and $y(t)$ the output. Thus, in a TV system, channel distortion varies as a function of time.

The behavior of a time variant system in the frequency domain can be obtained

by taking the Fourier transform of $h(t,\tau)$ with respect to time t, that yield the spreading function in 2.3:

$$S(\tau, v) = \int_{-\infty}^{\infty} h(\tau, t) e^{(-2\pi \mathrm{i} v t)} \mathrm{d}t \tag{2.3}$$

To better understand the meaning of the spreading function, it is useful to rewrite the 2.2 in terms of the latter. This can be done by deriving the inverse of 2.3 and substituting it in 2.2. $y(t)$ can thus be rewritten as follows:

$$y(t) = \int_{-\infty}^{\infty} \int_{-\infty}^{\infty} S(\tau, v) x(t-\tau) e^{(2\pi \mathrm{i} v t)} \mathrm{d}\tau \ \mathrm{d}v \tag{2.4}$$

From 2.4 y(t) appears as a weighted sum of delayed and frequency-shifted replicas of the transmitted signal. It means that the spreading function can be used to get an idea of the degree of delay and Doppler spreading that a signal experiences when traversing the channel. Such analysis can be carrier out by analysing the extent of $S(\tau, v)$ on the τ and v plane.

Another useful function that can be used to get information about the channel characterises is the scattering function $P(\tau, v)$ in 2.5:

$$P(\tau, v) = \mathrm{E}[|S(\tau, v)|^2] \tag{2.5}$$

By integrating the latter with respect the frequency shift, the power delay profile (i.e. the multipath intensity profile) can be obtained:

$$P_{\mathrm{d}}(\tau) = \int_{-\infty}^{\infty} P(\tau, v) \mathrm{d}v \tag{2.6}$$

While, by integrating the 2.5 over time delay, the Doppler power spectrum in 2.7 can be obtained:

$$P_{\mathrm{D}}(v) = \int_{-\infty}^{\infty} P(\tau, v) \mathrm{d}\tau \tag{2.7}$$

The Fourier transforms of $P_d(\tau)$ and $P_D(v)$ characterize the coherence bandwidth and coherence time of the channel, respectively. It should be noted that scattering function $P(\tau, v)$ in 2.5 is obtained under the wide-sense stationary uncorrelated scattering (WSSUS) assumption, according to the $h(\tau, t)$ is assumed to be stationary with respect to observation instant t and uncorrelated with respect to delay τ.

For many underwater channels, the WSSUS assumption is not satisfied, since the underwater channels are typically non-stationary in time and/or correlated in delay. However, in some cases, the channel behavior satisfied the WSSUS assumption during a specific time period and frequency range. In this case, it is said that the channel can be defined as quasi-WSSUS and that the long-term behavior of the channels cannot be described by a single scattering function, but repeated estimates should be made to describe it.

2.1.5 High propagation delays

The propagation speed of an electromagnetic wave in air is of the order of $3 \cdot 10^{-8}$ m/s, while that of a sound is about 330 to 340 m/s; in water, the latter propagates faster, with an average speed of 1500 m/s. This is about 5 orders of magnitude lower than the speed of a radio wave in the air. This results in high propagation delays. The speed of sound is not constant at every point in space: in fact, it increases with the increase of three parameters, namely temperature, salinity and pressure. However, depth is often used instead of pressure, since as the depth increases, the pressure increases linearly according to Stevin's law (on the seabed, it can even reach values of hundreds of atmospheres). Temperature and salinity levels vary with latitude, season, time of day, weather conditions and other oceanographic factors; however, it has been verified through experimental data that as depth increases, these values vary much more slowly. The relationship linking sound speed, depth, temperature and salinity level is extremely complex: it was empirically derived by Del Grosso (1974). For practical purposes, approximate equations are often used. One of these is the one by Medwin (1975), which is valid for temperatures between 0 and 32 degrees Celsius, a water salinity level between 22 and 45 ppt (parts per thousand), and depths less than 1000 m (from H. Medwind, C.S. Clay, Fundamentals of acoustical oceanography, Academic, San Diego 1997.):

$$v = 1449.2 + 4.6T - 0.055T^2 + 0.00029T^3 + (1.34 - 0.01T)(S - 35) + 0.016z \quad (2.8)$$

where

- v - speed of sound (m/s)

- T - temperature (°C)
- S - salinity level (ppt)
- z - depth (m)

With the above constraints, this formula gives an error of about 0.2 m/s compared to Del Grosso's formula. Another approximation example is that by Mackenzie (1981), which gives an error of 0.07 m/s and has constraints of temperature between 0 and 30°C, salinity level between 30 and 40 ppt, and a depth between 0 and 8000 m:

$$\begin{aligned} v = {} & 1448.96 + 4.591T - 5.304 \cdot 10^{-2}T^2 \\ & + 2.374 \cdot 10{-}4T^3 + 1.340(S - 35) + 1.630 \cdot 10^{-2}z \\ & + 1.675 \cdot 10{-}7z^2 - 1.025 \cdot 10^{-2}T(S - 35) - 7.139 \cdot 10{-}13Tz^3 \end{aligned}$$

The need for equations that accurately calculate the speed of sound in the sea, as well as quantify transmission delay times, is critical for certain types of applications, such as localization and synchronization. To study the speed of sound in water, one can also subdivide the transmission medium into different levels, generally according to depth, each of which is affected by particular effects and possesses specific properties. In deep water, a possible subdivision is as follows:

- surface level: the level closest to the water surface and the only one sensitive to changes in heat or cold and wind;
- seasonal thermocline: in this level, the seasons are assumed to influence the temperature (in some seasons it merges with the surface level). The velocity of sound propagation decreases as depth increases;
- main thermocline: also in this level, the sound speed decreases with increasing depth, but is little affected by seasonal changes. At the end of this level, the sound speed reaches its minimum;
- isothermal deep level: has a temperature that is assumed to be constant (about 4°C) and the speed of sound increases with depth. At high latitudes, this level tends to extend almost to the sea surface.

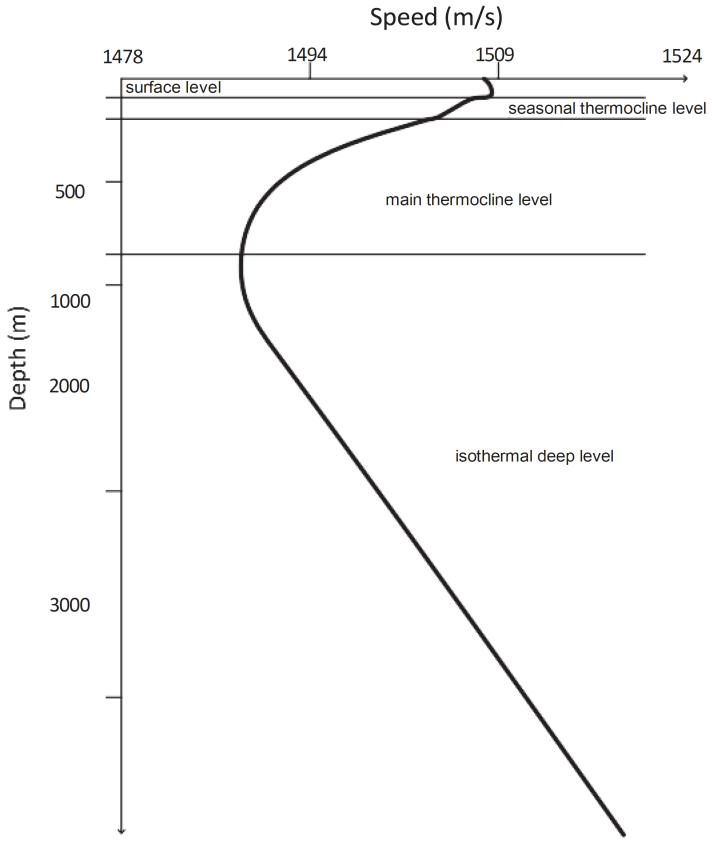

Figure 2.2: Example of Sound Speed Profile and subdivision into levels for a deep water scenario.

Figure 2.2 shows the sea-level subdivision for a common deep-water scenario and the associated Sound Speed Profile or SSP, which is a profile of the speed of sound along the water depth. For shallow water, on the other hand, sound speed is strongly influenced by heat or cold at surface, salinity changes, and currents. Because of the frequent variations in these parameters, the levels are numerous and poorly definable, as they quickly vary in time. Figure 2.3 shows several measurements of the sound speed profile as a function of depth near the coast of Kauai Island (Hawaii, USA) for shallow water (100 m).

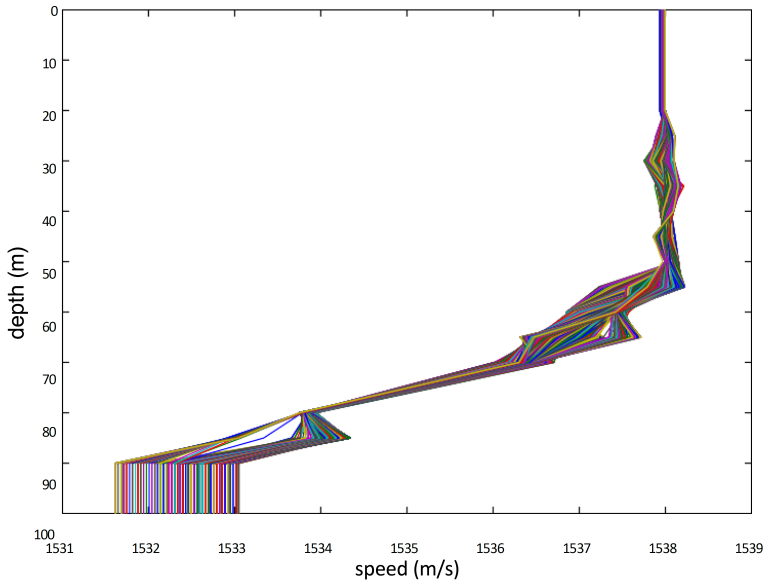

Figure 2.3: Examples of various Sound Speed Profiles for shallow waters (100 m).

2.1.6 Attenuation

The attenuation a of a channel is defined as the power ratio of a signal transmitted P_s over the useful signal received P_x:

$$a = \frac{P_s}{P_x} \tag{2.9}$$

The attenuation represents the loss in power due to phenomena such as absorption (i.e., the energy is transformed into heat) and scattering. This process depends on the carrier frequency: the higher the frequency, the greater the attenuation. Attenuation can therefore be considered as a function of two parameters: frequency (f measured in kHz) and distance (d measured in km). It is expressible as a product of two terms:

$$a(d, f) = d^k \cdot [\alpha(f)]^d \tag{2.10}$$

or in dB:

$$a^{dB}(d, f) = k \cdot 10log(d) + d \cdot \alpha^{dB}(f) \tag{2.11}$$

where

- $k \cdot 10log(d)$ is the spreading loss, and
- $d \cdot \alpha^{dB}(f)$ is the absorption loss.

The coefficient, k, called the dispersion coefficient and represents the geometry of propagation: 1 for cylindrical and 2 for spherical. The intermediate value of 1.5 is often used for analytical treatment. In addition, $\alpha(f)$, called the absorption coefficient, plays a key role and its approximate expression, derived empirically by Thorp, is:

$$\alpha^{dB}(f) = 10^{-3}\left[0.11\frac{f^2}{1+f^2} + 44\frac{f^2}{4100+f^2} + 2.75 \cdot 10^{-4} f^2 + 0.003\right] \text{dB/m} \quad (2.12)$$

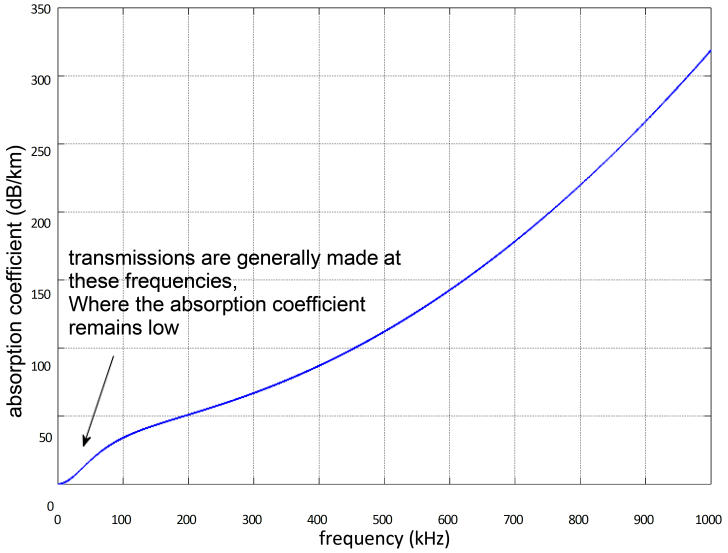

Figure 2.4: Absorption coefficient $\alpha^{dB}(f)$ as a function of frequency.

The approximation function, valid for frequencies above 100 Hz, is depicted in Figure 2.4. The absorption coefficient, expressed in dB, depends quadratically on the frequency if it is sufficiently high. This represents a strong limitation for the transmission frequency and, consequently, also for the bandwidth. The latter directly affects the transmission rate: having a bandwidth of the order of a few kHz means that only low transmission rates are available. Figure 2.5 shows the attenuation as a function of frequency for different sample distances. For high

frequencies, the dB values increase greatly; the effect is even more pronounced for longer distances. Figure 2.6 shows the attenuation as a function of distance from the transmitter and depth, in colored scale. This attenuation was calculated based on Bellhop, which is a simulator program capable of calculating attenuation and other parameters of propagation (see Section 4.1). In particular, the figure shows a deep water scenario (5 km), where the transmitter, placed at a depth of 1 km, transmits in a cone of 26 degrees. Note the existence of several shadow zones, depicted in white, and convergence points, where for a fixed distance from the transmitter the attenuation is lower, e.g. at 50 km (and 1 km deep) or 70 km (and 1.5 km deep).

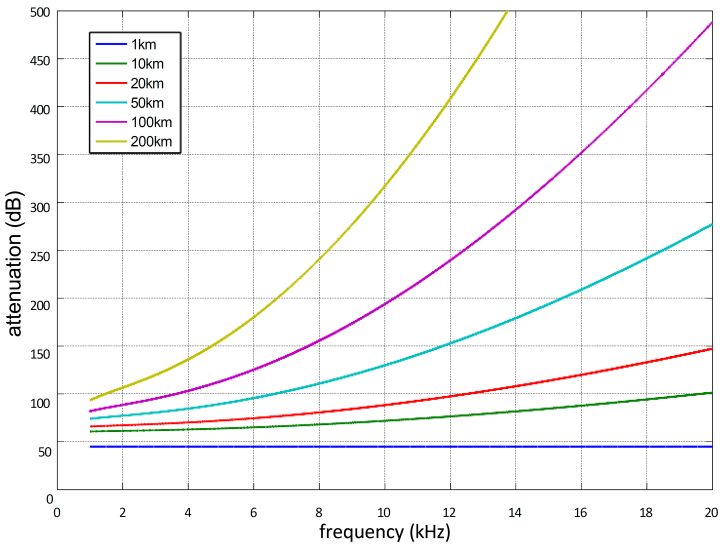

Figure 2.5: Attenuation $a^{dB}(d, f)$ as a function of frequency for different distances.

2.1.7 Power spectral density and signal-to-noise-ratio

The Power Spectral Density (PSD) gives information on how the statistical power of noise is distributed at different frequencies. By definition:

$$P_n = 2 \int_B N df \tag{2.13}$$

where:

- B is the operational bandwidth,

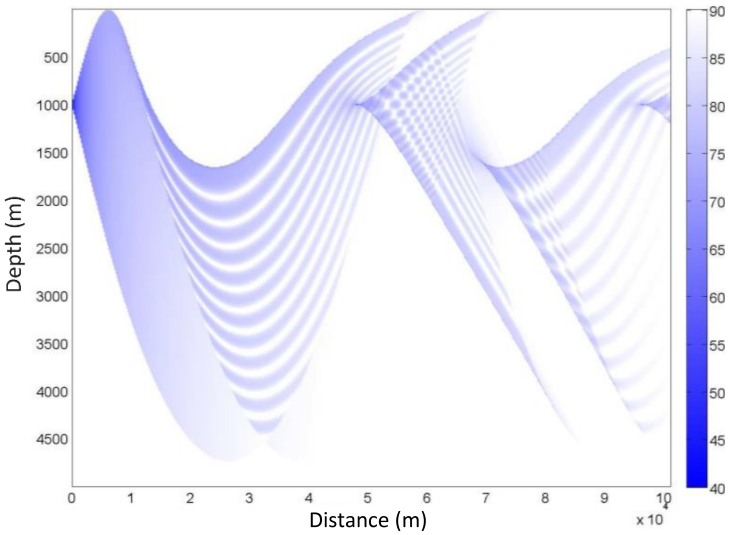

Figure 2.6: Sound attenuation as a function of distance from the transmitter and depth, for a deep water scenario.

- $P_n = E[|n|^2]$ is the (statistical) power of the noise n,
- N is the PSD of the noise n.

For the determination of the signal-to-noise-ratio (SNR) it is necessary to calculate the PSD of noise n. Noise is neither white (PSD not constant) nor Gaussian (its probability density is not a normal distribution), however, it is often decomposed as the sum of four components that are considered Gaussian: turbulence (N_t), shipping (N_s), wind and surface waves (N_w), and thermal noise at the receiver (N_{th}). The dB values of the various noise components are:

$$
\begin{aligned}
N_t^{dB}(f) &= 17 - 30log_{10}(f) \\
N_s^{dB}(f) &= 40 + 20(S - 0.5) + 26log_{10}(f) - 60log_{10}(f + 0.03) \\
N_w^{dB}(f) &= 50 + 7.5\sqrt{W} + 20log_{10}(f) - 40log_{10}(f + 0.4) \\
N_{th}^{dB}(f) &= -15 + 20log_{10}(f)
\end{aligned}
$$

where:

- S is the shipping factor (between 0 and 1) and represents the shipping intensity on the surface of the water,

- W is the wind speed in m/s.

All these four components, converted to linear, are measured in $\mu Pa/Hz$. The sum gives the total PSD:

$$N(f) = N_t(f) + N_s(f) + N_w(f) + N_{th}(f)$$

Figure 2.7 shows in black the PSD of the channel noise for different values of shipping factor and wind intensity. The PSDs of the four components are also shown. Note that these have different impact at different frequencies (considering S = 0 and W = 0 m/s):

- for low frequencies (up to about 10 Hz) the dominant effect is turbulence;
- for frequencies, approximately between 10 Hz and 300 Hz, the dominant effect is shipping intensity;
- for frequencies between 300 Hz and 40 kHz approximately, the dominant effect is given by wind and surface waves. This is the most important region since acoustic transmissions occur at such frequencies;
- for frequencies above 40 kHz, the dominant effect is thermal noise, due to the receiver circuits.

The calculation of the signal-to-noise ratio (SNR) can be computed by using the definitions of noise power density and attenuation presented so far. In particular, we consider the useful power, P_x, of the transmitted signal and the noise power P_n. The former can be derived by recalling the definition of attenuation and assuming, in an analytical study, that the transmitted power P_s is constant since it is dependent on the transmitting antenna. The power of noise, on the other hand, can be derived by definition from its power spectral density. Thus, assuming the PSD of the noise constant in a narrow band, B_0 , around f_0 , the SNR, Γ, can be expressed as:

$$\Gamma(d, f_0) = \frac{P_x}{P_n} = \frac{P_s/a(d, f_0)}{N(f_0) \cdot 2B_0} = \frac{P_s}{N(f_0) \cdot 2B_0 \cdot a(d, f_0)}$$

It is often interesting to solve the following optimization problem: given a distance, find the frequency, f_{opt} , that maximizes the SNR. Such a frequency can be

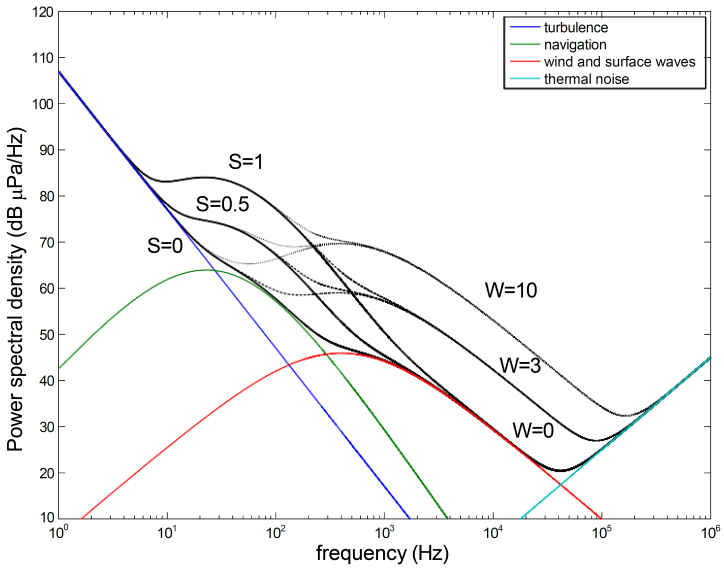

Figure 2.7: Power spectral density of noise (in black) for different values of shipping and wind intensity. In colors, the four components of the noise PSD.

referred as optimal. Analytically, for a given d, to maximize the SNR we should calculate:

$$\min_f \{N(f) \cdot a(d, f)\}$$

Figure 2.8 shows in black the curves $\frac{1}{N(f)a(d,f)}$ as a function of frequency for different values of d (ranging from 10 m to 100 km). Each of these curves exhibits a maximum, marked by the thick black line. The blue and red curves define the 3-dB band. This represents a range of frequencies within which the SNR remains sufficiently high (at least half of the optimal frequency). This band is $B_{3dB}(d) = f2(d) - f1(d)$, with $f1(d)$ and $f2(d)$ are such that:

$$\Gamma(d, f1(d)) = \Gamma(d, f2(d)) = 0.5\Gamma(d, f_{opt}(d))$$

From the figure it is clear that both the optimal frequency and bandwidth decrease as the distance increases. Thus high transmission rates are more sustainable at short distances because the bandwidth is wider and the optimal transmission frequency is higher. In contrast, for long distances, the channel capacity decreases.

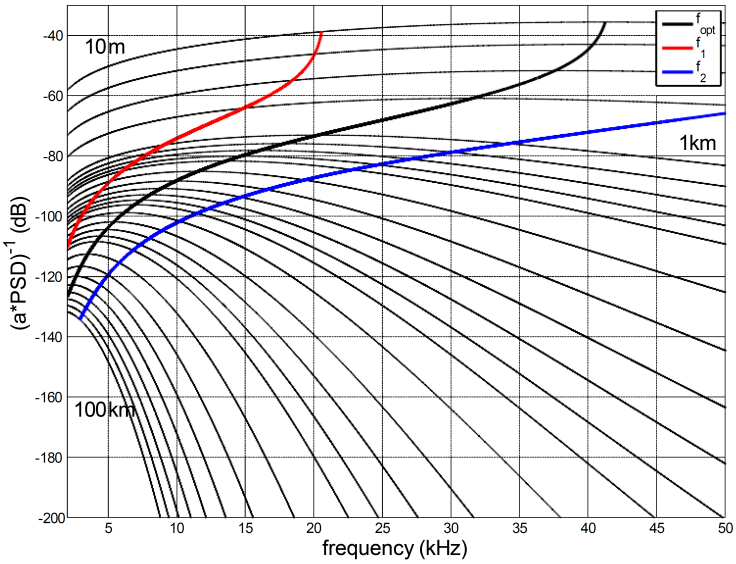

Figure 2.8: Trend of factors $\frac{1}{N(f)a(d,f)}$. In red and blue are the curves defining the 3dB band, in black the curve defining the optimal frequencies. The parameters used are S = 1, W = 0 m/s, k = 1.5

Chapter 3

Robust modulation in underwater acoustic communications

3.1 JANUS Standard

In the literature, a plethora of underwater acoustic modems has been developed to meet the needs of different applications (see [10] and citations therein). However, the absence of a common standard for underwater communications has led to the development of several manufacturer-specific devices, generally employing proprietary modulation schemes. To overcome this lack of interoperability, the NATO Centre for Maritime Research and Experimentation (CMRE) has developed and established in March 2017 a first standard for underwater communications, named JANUS [6]. The proposed protocol is not intended to be limited only to NATO military use, but also for civilian and NON-NATO maritime assets, because it has been designed both to ensure communication interoperability between heterogeneous assets and to minimize the changes required to bring existing underwater communications equipment into compliance. Indeed, in [11] JANUS is proposed as a second "language" to be implemented in manufacturer-specific devices in parallel with their proprietary digital coding schemes: JANUS could be used to establish the first contact, notifying the presence of an asset in the area and its capabilities to negotiate communication parameters. Subsequently, the devices can switch to a suitable modulation scheme supported by all or a subset of the devices in the area.

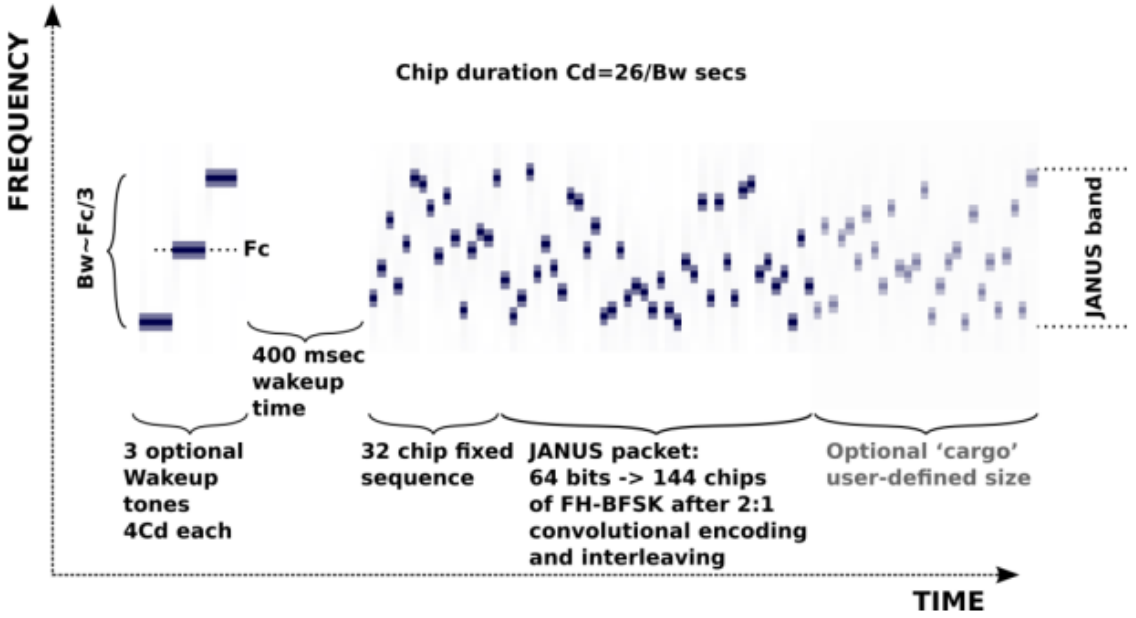

Figure 3.1: Time-Frequency structure of a JANUS packet.

JANUS uses a simple FH-BFSK (Frequency-Hopped Binary frequency-shift keying) modulation scheme in which binary data is mapped to 13 evenly-spaced tone pairs spanning the bandwidth B_w of the transmission, which is nominally 1/3 of the central frequency F_c. Although it is expected that in the future other bands will be proposed in order to use the JANUS standard in various applications, to date the initial frequency band allocation ranges from $9440Hz$ to $13600Hz$, with a central frequency of $11520Hz$. The Chip Duration C_d and the Frequency Slot Width F_{Sw}) are directly calculated from the upper and lower band values. Other parameters, such as the Frequency Hopping sequence, remain constant for any chosen band.

The JANUS packet starts with a fixed preamble of 32 chips, i.e. 32 frequency-hopped symbols, whose value is set to a pseudo-random m-sequence. This preamble is followed by a "baseline JANUS Packet" encoding 64 bits of information. Optionally, a "Cargo" packet of arbitrary length can be added at the end. In addition, in order to also include an energy-saving mechanism in JANUS communications, three tones can precede the entire packet to wake a modem from a power-saving sleep state.

The robustness to temporal and frequency fading is provided by a 2:1 convolutional coding redundancy with a constraint length of 9, using the following polynomial generators:

$$\begin{aligned} g_1(x) &= x^8 + x^7 + x^5 + x^3 + x^2 + x^1 + 1 \\ g_2(x) &= x^8 + x^4 + x^3 + x^2 + 1 \end{aligned} \tag{3.1}$$

The coded signal is then followed by interleaving. The baseline packet and the cargo are always separately encoded and interleaved as the baseline packet needs to be decoded to know how many bytes are in the cargo.

Error checking of the "baseline JANUS Packet" is performed using an 8-bit CRC (Cyclic Redundancy Check) which uses the polynomial $p(x) = x^8 + x^2 + x^1 + 1$, initialized to 0.

3.2 Sweep-Spread carrier method

The sweep-spread carrier (S2C) modulation has been presented by Kebkal et al. in [8] as a robust and reliable communication method for transmitting acoustic signals in underwater communication channels commonly affected by severe multipath and Doppler effects. The main innovation brought by this communication method is the use of a non-conventional carrier signal to convey the modulated data through the underwater channel. This special waveform, as opposed to the conventional single-frequency carrier signal, consists of a signal that periodically spans the whole available frequency band from the lowest frequency f_L to the highest frequency f_H. As shown in the figure 3.2, such carrier signal is nothing more than a sequence of linear chirps with no interval gap, whose instantaneous frequency can be expressed by means of a sawtooth equation. Indicating with T_{SW} the sweep duration (i.e. the time interval required to span the entire bandwidth) and with k the sweep rate, the analytic expression in complex form of a sweep-spread carrier can be expressed as follows:

$$c(t) = e^{\left[j\left(2\pi f_L\left(t - \left\lfloor \frac{t}{T_{SW}} \right\rfloor T_{SW}\right) + k\left(t - \left\lfloor \frac{t}{T_{SW}} \right\rfloor T_{SW}\right)^2\right)\right]} \tag{3.2}$$

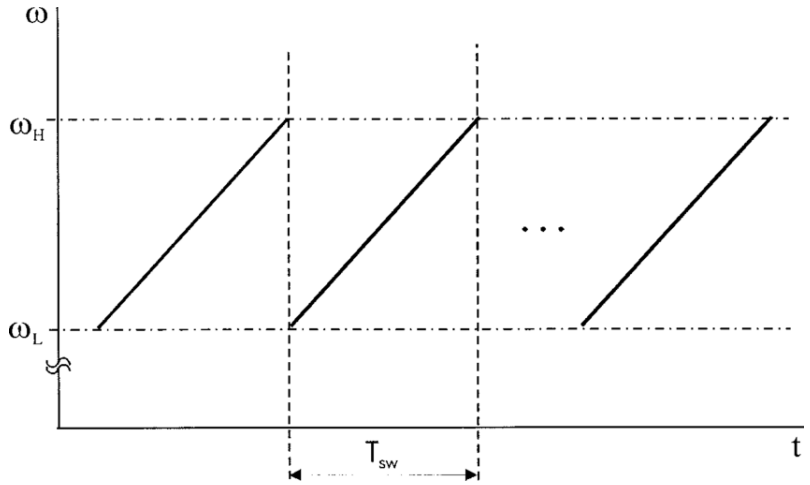

Figure 3.2: Sweep-spread carrier consisting of a sequence of up-chirp with no separation gap [8]

where $\lfloor . \rfloor$ stands for the floor operand (i.e. the closest lower integer) and the sweep rate k is defined as

$$k = \frac{\pi(f_H - f_L)}{T_{SW}}. \tag{3.3}$$

The main advantage, as well as the goal for which this method was designed, lies in its multipath interference rejection capability without resorting to very complex signal processing algorithms. When a signal is transmitted along the underwater channel, it reaches the receiver through different paths due to reflections from the bottom, sea surface or any other objects present in the environment such as a ship's hull. Consequentially, as shown in figure 3.3, at receiver side, the signal arrives as sum of different time-shifted and attenuated versions of the transmitted signal.

The signal structure of the S2C modulation allows for splitting the multipath components of the received signal in the frequency domain by means of the despreading transformation. This simple operation consists in multiplying the received signal with a reference signal having the same sweep period and the same (inverse) slope of the transmitted signal. The result of this despreading transformation is that the frequency variations of the S2C waveform are removed from the received signal and the time-delayed multipath arrivals appear as separate spectral lines in the frequency domain. At this point and using proper algorithms, each of these spectral lines can

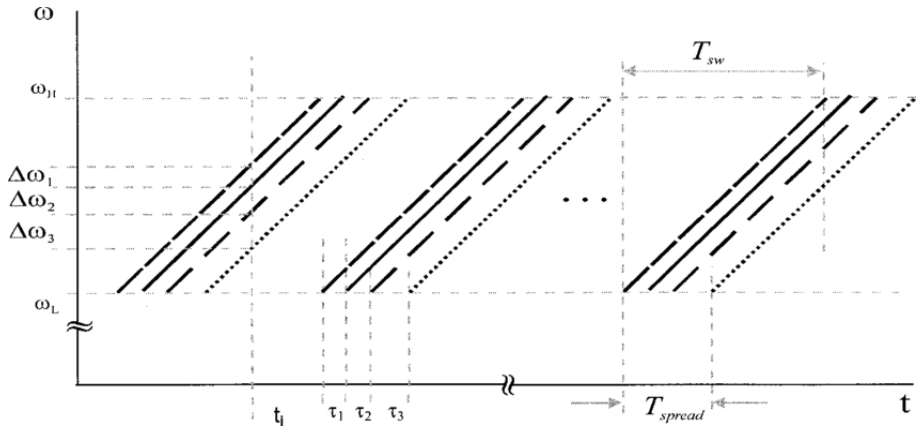

Figure 3.3: Sweep-spread carrier after multipath propagation in UW channel [8].

be identified and separately processed by means of common filter operations.

Figure 3.4 shows the effect of the despreading transformation on the received signal. More specifically, figure a) shows a drawing of how the received signal could look after having propagated along different paths. Each sweep represents a single time-shifted multipath arrival and the different lines have been used to indicate different levels of attenuation. The solid line represents the strongest path, i.e. the one with the most energy. Figure b) shows the signal used in [8] for the despreading operation, while Figure c) shows a drawing of how the received signal looks after the despreading transformation and if a perfect timing between the strongest signal and the signal used for the despreading transformation has been assumed.

Although this method theoretically allows in an ideal case an easy separation of the multipath arrivals, in non ideal conditions some limitations are inevitable and hence some requirements should be respected. The main limitation arises in presence of doppler effect. In this case, it is well known that the signal will be shifted as well as dilated/compressed in the frequency domain. Consequentially, if the doppler distortion experienced by each propagation path exceeds certain limits, the multipath arrivals could interfere with each other. The general requirement that ensures any interference between multipath arrivals is given by $\Delta\omega_i >> \omega^i_{dmax}$. This condition can be achieved by acting on the sweep slope: the steeper the slope, the better the multipath resolution. In [8] authors proposed an additional procedure that

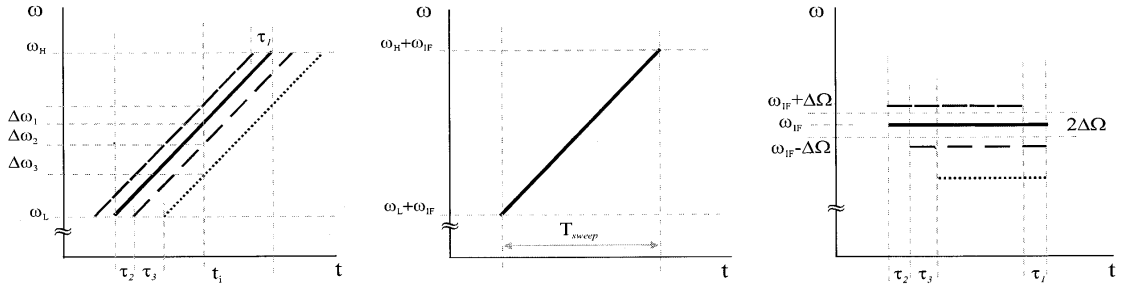

(a) A single sweep as part of a Sweep-spread carrier with four multipath arrivals

(b) Despreading signal

(c) Despreaded signal

Figure 3.4: Despreading [8]

allows to define the modulation parameters that best match the channel conditions and hence ensure a sufficient quality in the separation of the multipath components. This procedure was applied by the authors during real tests in shallow water channels of a lake and in the Baltic Sea and was performed by transmitting a channel probe before the transmission. The channel probe consisted of three pulses separated by half their duration and the procedure was intended to analyze the multipath structure and the energy associated with each spectral line. As a result of this investigation, a feedback message was retransmitted to the transmitter, in order to redefine the initially used sweep slope.

3.3 Modulation schemes for sweep-spread carrier

To the best of our knowledge, all the works present in literature use a differential Q-PSK (quadrature phase shift keying) as coding schemes to modulate the sweep-spread carrier. In [8], that is the original work in which the sweep-spread carrier was proposed and its feasibility has been proved, authors use a differential Q-PSK modulation schemes to code 10 symbols, each of 1 ms duration, on a sweep-spread carrier spanning the frequency band between 42 kHz and 82 kHz with a sweep cycle

of 10 ms. As a result, the frequency gradient is equal to 4 kHz/ms and the bit rate is equal to 2 kbps. In [12], authors use differential Q-PSK to code a total of 1024 symbols in a sweep-spread carrier spanning the frequency band between 18 kHz and 34 kHz with a sweep duration of 210 ms and a symbol spacing of 1.5 ms. In this case, the authors say they used a root-raised-cosine pulse shaping with a roll-off factor of 0.2. Moreover, a BCH encoder was used to encode the information bits. In [13] also a differential Q-PSK modulation scheme has been used and different parameter combinations have been used in their simulations.

3.4 Frame structure and synchronization for Sweep-spread carrier system

In [8], the transmitted signal was composed of a short and uncoded preamble followed by a data packet in which information bits were coded onto the sweep-spread carrier with the DQPSK modulation scheme. The short preamble consists of a series of sweeps. It is used for synchronization purposes and the timing estimation is performed in two steps. In the first step, a coarse time alignment is performed by finding the main multi-path arrival i.e. the spectral tone with the largest energy concentration. In the second step, a fine timing alignment is carried out in order to obtain a more accurate timing estimation. In [12], the same packet structure consisting of a preamble followed by a data packet is transmitted. However, in this case, the preamble consists of a sweep-spread carrier modulated with known pilot symbols and it is employed for carrier and symbol synchronization/tracking purposes. More specifically, as a first step, the preamble is detected and then a channel impulse response estimation is performed. This procedure allows to identify the times of arrival of the preamble signal from the strongest paths and also to estimate the complex-valued gains relative to all the resulting channel paths, later used to improve the detection stage. In [13] the frame structure is composed of a data packet surrounded by a preamble and a postamble signal. Both the preamble and postamble consist of a single unmodulated sweep and are used for synchronization, channel estimation and doppler correction. A guard interval after the preamble and before the postamble is inserted to facilitate channel estimation.

3.5 Sweep-spread carrier receivers

Since the Sweep-spread carrier method has been presented in [8], some variants of the initial S2C receiver scheme have been proposed. Each of these reception schemes aims to make better use of the potential of the Sweep-spread carrier method. As anticipated in section 3.2, the main advantage of the sweep-spread carrier method consists in the possibility of separating multipath arrivals in the frequency domain without using complex processing in the time domain. Indeed, by multiplying the received signal by a sweep signal having the same sweep period and the same slope as the transmitted signal (despreading transformation), the multipath arrivals appear as spaced spectral lines that can be isolated from each other with a conventional band filter process. After that, the demodulation process to extract the information bits can be started. However, for the despreading operation to be successful, a preliminary timing estimation must be carried out. Indeed, in order to correctly remove the frequency variation from the sweep-spread carrier, the multiplication between the received signal and the reference one must be executed in a synchronous way. It means that the reference signal must be time-aligned with the main multipath arrival, i.e. the multi-path arrival with the greatest energy concentration. The timing estimation is generally carried out during the preamble processing and the specific alignment algorithm to be used depends on the chosen preamble waveform.

In the original work [8], the receiver scheme exploits only the received signal coming from the strongest path to perform demodulation. During the preamble processing, the timing estimation of the strongest multi-path arrival is obtained according to the maximum likelihood estimation principles. More specifically, the coarse alignment is performed by scanning the received signal with a filter in search of the spectral line holding the greatest energy content. Then, a fine timing estimation is accomplished in order to eliminate the uncertainty of the coarse estimation that depends on the window size filter. Once the timing estimation is terminated, the synchronous despreading is executed. In this specific case, authors execute a heterodyne despreading. It means that, as reference signal, they use a sweep-spread carrier with the same slope and the same period as the transmitted signal. However, the initial frequency of the reference signal is 10 kHz lower than the transmitted one. In this way, an intermediate-frequency spectrum is obtained and the main spectral

line is filtered from it. Once the frequency variation is eliminated, the demodulation process that extracts the information bit from the DQPSK coded symbols starts. Although the authors assert that thanks to the suppression of the time-varying multipath arrivals (i.e. the filtering of multipath arrivals different from the strongest one), a PLL local oscillator could be used without severely compromising the loop stability, in their test they apply a simple differential QPSK receiver and the symbols are correctly demodulated. In the patent document [14], the same authors present some schematic receiver architectures with more than one processing branch that seem to make use of multipath signals (perhaps the strongest ones) to improve the subsequent decoding stage. However, not much technical information is provided, so for example, it is not clear how the different multipath arrivals are synchronized and combined together. In [12], a more detailed receiver architecture for S2C communications is presented. This receiver, which follows the structure of a rake receiver, is designed to exploit not only the most powerful multipath arrival but a certain number of propagation paths with significant energy levels.In their work, the authors refer to it as a "multi-branch" S2C receiver scheme and demonstrate an increase in the power system efficiency with respect to a single-path-based S2C receiver (intending with this last term, the receiver structure in [8]). This S2C multi-branch receiver architecture is developed to exploit not only the most powerful multipath arrival but a certain number of propagation paths with significant energy levels. To do this, the not negligible multipath arrivals are first identified and then individually processed by each of the parallel receiver branches. Finally, the branch outputs are optimally combined according to the maximal ratio combining (MRC) criterion. As in [8], a preliminary synchronization stage (and not only) is executed before the operation described above. This synchronization stage is carried out during the preamble processing and serves to estimate the timing of the arrival of the strongest multipath signals that have been processed by the parallel branches. In addition to this, a channel impulse response estimation is also performed in order to estimate the (complex-valued) gains of the different strongest multipath signals. The timing estimations are performed in order to generate the reference signals synchronously (each synchronous with a single multipath signal selected from the reception process). Instead, channel impulse response estimation is performed not only to identify the strongest paths but also to correctly apply the

MRC technique. Both of the aforementioned operations are accomplished by means of a correlation procedure followed by a maximum-search algorithm. The latter is a threshold algorithm based on the SNR estimation that attempts to better classify the strongest multipath arrivals from any kind of interference (whether it's a false peak or a sidelobe of some strongest multipath arrival) and discard multipath arrivals and discard arrivals whose differential delay is too small to ensure adequate separation. Another aspect that distinguishes the S2C receivers presented in [8] and [12] concerns the characteristics of the reference signals used for despreading. In fact, in [12] authors do not use a heterodyne conversion but a baseband conversion. In [13], authors try to improve the S2C communication method by acting on the decoding stage of a S2C receiver. More specifically, they propose a new variational soft symbol decoding (VSSD) algorithm based on the principle of variational Bayes' inference.

Chapter 4

Simulation and experimental platforms

In any research area, simulation and experimentation represent a crucial and essential step in the research and development chain. In the specific case of underwater communications, in-field testing is not a trivial task. For their implementation, experiments both in shallow and very deep waters can require the use of many resources, often at a high cost. For their implementation, experiments in shallow or very deep waters can be really demanding in terms of both logistical and economic resources. Therefore, sea trials are almost always conducted as a final validation step when the system to be tested is mature enough to justify the effort. For this reason, simulation is still the primary validation tool used to test underwater acoustic communication systems before any in-field trials. However, due to the great variety of existing submarine environments and application scenarios, together with the unpredictable variability of channel conditions as a function of meteorological factors and seasonal climate changes, it is really difficult to have a simulation platform that is able to take all these aspects into account. Consequently, various efforts have been made in an attempt to model the underwater channel, and various simulation methodologies have been proposed in order to make the simulation experiments as realistic as possible. In this chapter, we give a brief overview of the experimental and simulation platforms used in this work.

4.1 Bellhop

BELLOP is beam tracing software developed to predict sound pressure fields in marine environments. It is released as part of the Acoustics ToolBox [15] and is widely used to simulate realistic underwater sound channels. The core program is written in FORTRAN and released with a set of Matlab utilities that allow you to both easily run the program and view the outputs. Being a ray tracing program, the computation of the acoustic pressure field is based on the assumption that the sound propagates along normal rays at the wave fronts (i.e. the surfaces of the acoustic wave with constant phase). This implies that an acoustic source is approximated by a range of rays traveling along the medium. The algorithm works by associating each ray with a specific beam profile and tracing the propagation of each beam through different paths. The trajectories of these paths depend both on the sound velocity profile and on the interaction between the rays and the boundaries (i.e. sea bottom and sea surface) of the environment. More specifically, the sound velocity profile mainly acts on the curvature of the rays, while the ray-boundary interactions mainly affect the ray's reflection angle. The acoustic pressure at a specific point in the plan is calculated by adding the contributions of the beams. The user can select different types of beams, including Gaussian and hat-shaped beams, with both geometric and physics-based diffusion laws. Compared to standard ray tracing, beam tracing has the advantage of not producing some artifacts such as perfect shadows and caustics [16]. Before starting the simulation, it is necessary to set the characteristics of the environment and the geometry of the scenario. This information must be provided through various files according to the user guide [17]. The basic simulation requires only one file, the so-called "environmental file", through which the user can specify the main environmental parameters such as the sound velocity profile (SSP), top and bottom reflection coefficients, etc. The same file is used to specify scenario information such as source and receiver locations, as well as the bottom depth and reception range. When only the environmental file is used, both the bottom and the surface are assumed as flat boundaries. In case of range-dependent bottoms or range-dependent surfaces, a bathymetry file and an altimetry file must be added.

BELLHOP can produce a variety of useful outputs depending on the "run type" set by the user in the environmental file. These file outputs include the ray tracing,

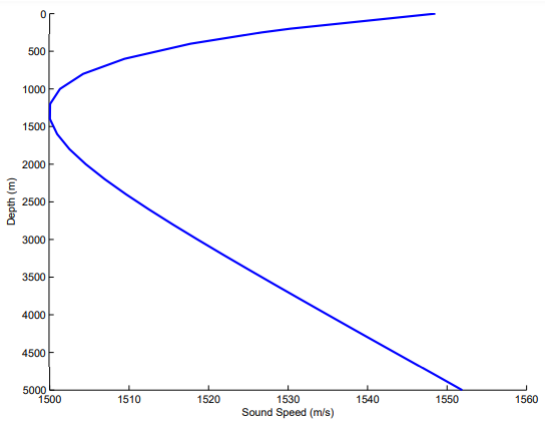

Figure 4.1: Munk sound speed profile

the transmission loss and the echo arrivals.Ray tracing can be used to get a view of how the energy propagates in the channel, while transmission loss can be used to get a view of how the sound intensity is distributed in the channel. For example, figure 4.2 shows the ray tracing and the coherent transmission losses obtained in a 5 km depth ocean when the Munk sound speed profile in figure 4.1 is considered. The Munk profile [18] is an idealized ocean SSP that allows to simulate the typical sound propagation in deep water. In its general form, the Munk profile is given as a function of depth by the following formula:

$$c(z) = 1500\left[1.0 + \epsilon\left(\frac{2(z-1300)}{1300} - 1 + e^{-\frac{2(z-1300)}{1300}}\right)\right]$$

where the quantity ϵ is taken to be $\epsilon = 0.00737$.

In figure 4.2a, different colors were used to differentiate the rays that do not interact with the boundaries (red line) from the rays that instead undergo multiple reflections with the sea bottom or surface (black line). Although this picture can be useful to get an idea of how sound travels along the channel, many considerations cannot be deduced about how these paths interfere with each other. This information can be deduced from figure 4.2b which shows the transmission loss (i.e. essentially the sound intensity due to a source of unit strength). It should be noted that the transmission losses are calculated for a single tone of a specific frequency in Hz (i.e. the one specified in the environment file). It means that the frequency

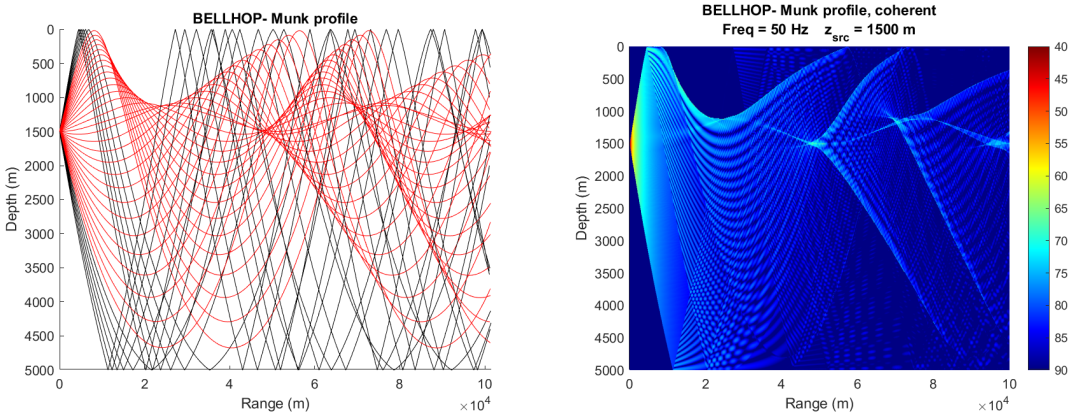

(a) Rays tracing

(b) Coherent transmission loss

Figure 4.2: Bellhop outputs considering a Munk SSP and a source depth of 1500 m

parameter has an important impact on the sound intensity computation since the interference pattern is directly related to the wavelength. Furthermore, the frequency also affects the attenuation when it is present. In the case of figure 4.2b a frequency of 50 kHz was used. Another useful and widely used Bellhop output is the "arrival file", which contains the channel impulse response information (i.e. the amplitudes, the phase and the travel times associated with each echo arrival) as well as other specific information (i.e. the ray take-off angle at the source and at the receiver and number of top and bottom bounces). According to the settings chosen by the user, all these informations can be calculated for a specific point (a single coordinate pair) or on a grid (multiple coordinate pairs) of the range-depth plan. Anyway, each of these points represents a virtual reception point and, for each of these, the channel impulse response at this specific location of the environment can be visualized. Figure 4.3a shows an example of a channel impulse response obtained at a range of 90.5 km and a depth of 1500 m, while figure 4.3b shows in detail the distribution of the second cluster of echo arrivals. The channel impulse response can be used to simulate the transmission of a signal through the acoustic channel by simply performing a convolution operation between the signal to be transmitted and the channel impulse response at the desired location. The Bellhop features described above are just some of those that this beam tracing software offers. The complete discussion of this simulation platform is not the aim of this work. The interested

reader can find more detailed descriptions starting from the references introduced during the description.

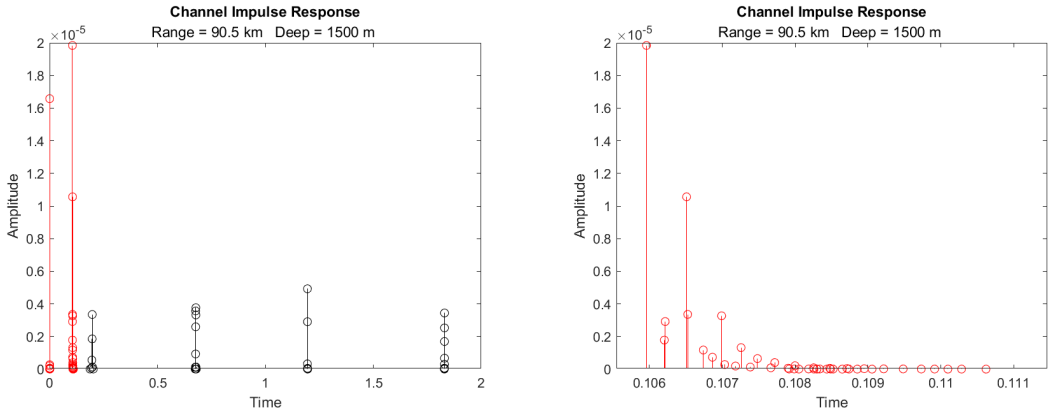

(a) Impulse response

(b) Detail of the second cluster

Figure 4.3: Impulse response at a range of 90.5 km and a depth of 1500 m

4.2 Watermark

The underWater AcousTic channEl Replay benchMARK (Watermark) [7] is a realistic simulation tool for testing the performance of physical-layer algorithms (e.g. detection and synchronization) or modulation schemes under realistic and reproducible conditions.

The simulator works on the basis of the channel replay principle, which consists of convolving the user signals with at-sea measurements of the time-varying impulse response. Matematically, this operation can be expressed as in 4.1:

$$y(t) = \int_{-\infty}^{+\infty} \hat{h}(t,\tau)\, x(t-\tau)\, \mathrm{d}\tau + n(t) \tag{4.1}$$

where x(t) is the input signal, $\hat{h}(t,\tau)$ is the channel time-varying impulse response (TVIR) estimate, n(t) is a noise term, and y(t) is the distorted output signal. In Watermark, the channel replay principle is applied in direct-replay mode. It means that the user signals are directly convoluted with the measured channel, which is an estimate of the true channel $h(t,\tau)$. This implies that the maximum simulation time

is bound by the channel measurement time. However, as reported in [7] and citations therein, it has the advantage of faithfully reproducing several channel effects (e.g. channel non-stationarity, correlated scattering, time-varying delays, etc) except for the overspread channel due to the difficult measurement. Moreover, it has been proven that simulated bit and packet error ratios, as well as receiver output signal-to-noise ratio (SNR), are close to the corresponding values measured at sea.

To start the simulation, the user's signal is passed as an input to Watermark. The simulator treats the input signal as a packet and makes multiple copies of it, as many as fit into the measured time-varying impulse response channel. To avoid reverb superimposition, a space between successive packets is inserted. Since the measured channel trace has a known finite length, the spacing is also known. The number of output packets returned by the simulation for a single time-varying impulse response channel is given by:

$$N = \lfloor T_{\text{play}}/(T_{\text{s}} + T_{\text{rep}} + \Delta) \rfloor \ . \tag{4.2}$$

Ts is the input signal duration, T_{play} the play time, T_{rep} the pulse repetition time of the channel sounder, and $\delta = 4ms$ a safety margin used to accommodate possible sidelobes occurring in the filtering process. Only in the case of SISO packets, can gaussian noise (AWGN) at a specified E_b/N_0 value be added during the simulation for a specific value of signal energy per information bit E_b and noise power spectral density N_0. The noisy waveform is $\approx 10s$ longer than the actual packet, which arrives with a random delay after $4 - 6s$.

Watermark is issued with a library of five channels measured in different sites of the world. Figure 4.4 represents a picture of the measurement setup for the five available channels. In more detail, in Norway-Oslofjord (NOF1) and Norway-Continental Shelf (NCS1) (Norwegians channels), both the transmitter and the receiver are bottom-mounted. These two channels use a single hydrophone receiver and are then single-input-single-output (SISO). In the Brest Commercial Harbor (BCH1, French channel), both the transmitter and the receiver are suspended in water close to the dock of the harbor. Since the receiver is composed of a hydrophone array, this channel is single-input-multiple-output (SIMO). In Kauai site (KAU1 and KAU2, Hawaiian channels) the transmitter is suspended in water and

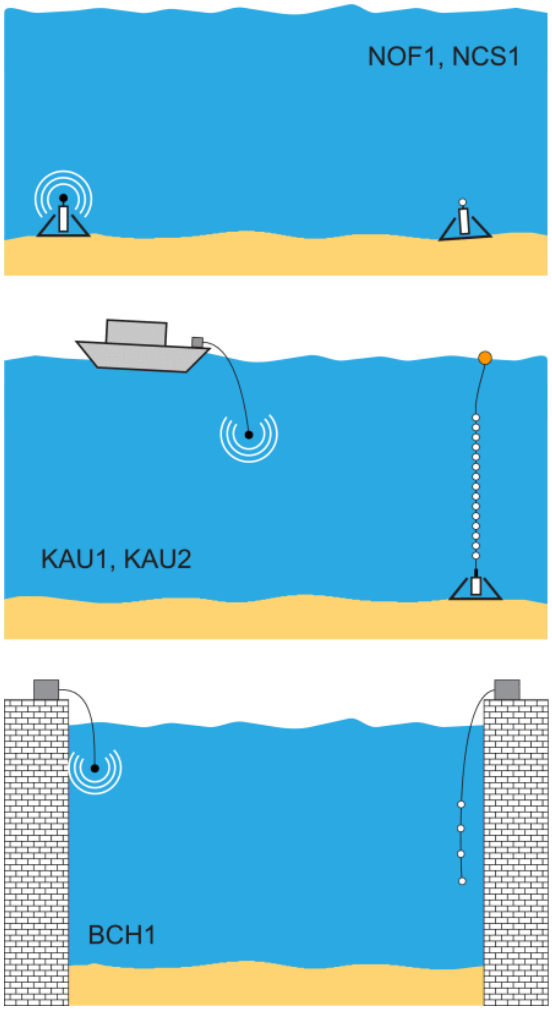

Figure 4.4: Deployment setup for Watermark channels sounding.

towed by a ship, while the receiver is bottom-anchored and suspended vertically through a buoy. Also in this setup, the receiver is composed of a hydrophone array and the channel is of the SIMO type. Table 4.5 summarizes all the characteristics of the channels.

The time-varying impulse response of the Watermark channel is obtained from the channel sounding procedure as described in [19]. The latter is performed by transmitting selected probing signals [19] and it can be used, not only to create archive files for channel simulators, but also to study different aspects of underwater acoustic channels, create realistic channel models and get channel parameters (e.g.

Name	NOF1	NCS1	BCH1	KAU1	KAU2
Environment	Fjord	Shelf	Harbor	Shelf	Shelf
Time of year	June	June	May	July	July
Range	750 m	540 m	800 m	1080 m	3160 m
Water depth	10 m	80 m	20 m	100 m	100 m
Transmitter depl.	Bottom	Bottom	Suspended	Towed	Towed
Receiver depl.	Bottom	Bottom	Suspended	Suspended	Suspended
Probe signal type	LFM train	Pseudonoise	Pseudonoise	LFM train	LFM train
−3-dB frequency band	10–18 kHz	10–18 kHz	32.5–37.5 kHz	4–8 kHz	4–8 kHz
Roll-off fact.	1/8	1/8	1/10	1/8	1/8
Sounding duration	32.9 s	32.6 s	59.4 s	32.9 s	32.9 s
Delay coverage	128 ms	32 ms	102 ms	128 ms	128 ms
Doppler coverage	7.8 Hz	31.4 Hz	9.8 Hz	7.8 Hz	7.8 Hz
Type	SISO	SISO	SIMO	SIMO	SIMO
# hydrophones	1	1	4	16	16
Element spacing	—	—	1 m	3.75 m	3.75 m
# cycles	60	60	1	1	1
Cycle time	400 s	600 s	—	—	—
Total play time	33 min	33 min	1 min	33 s	33 s

Figure 4.5: Characteristics of the Watermark channels.

doppler spread, delay spread, etc). Knowledge of the channel parameters can be useful to understand how these can affect the performance of a communication system or a specific modulation scheme.

The choice of the probing signals depends on the characteristics of the channel (if these are known in advance), on the type of signal processing used for the channel estimation and on the signal properties of the probe itself.

In the specific case of the Watermark simulator,the time-varying channel impulse responses were obtained by using two types of waveforms: linear frequency modulated (LFM) chirp trains and pseudorandom binary sequences (PRBS). The latter consist in the repetition of a sequence of bits of maximum length $c_m \in \{-1; 1\}$, modulated onto a binary phase-shift keyed waveform. Because of their good autocorrelation properties, both waveforms are commonly used for this purpose [7]. The mathematical expression of a single PRBS and a LFM pulse used to build the probing signal are respectively reported in 4.3 and 4.4:

$$p(t) = sin(2\pi f_c t) \sum_{m=0}^{M-1} c_m u(t - \frac{m}{M}T) \tag{4.3}$$

$$p(t) = sin(2\pi[(f_c - \frac{B}{2})t + \frac{B}{2T}t^2]) \tag{4.4}$$

where fc denotes the center frequency, B the bandwidth, T the duration, and $u(t)$ the pulse shape function. In both cases, the probing signal is composed of trains of these pulses, transmitted without any pause between them. Using N as the number of pulses in the train, the probing signal can be expressed as:

$$s(t) = \sum_{n=0}^{N-1} p(t - nT) \tag{4.5}$$

In addition, the probing signals were modeled through a raised root cosine filter using a specific but small roll-off factor in order to have a nearly rectangular spectrum. The estimated time-varying channel impulse response was obtained by passing the received probing signal through a filter matched to the transmit pulse of the probing signal. As a result, the series of impulse response estimates are stacked to provide a discrete matrix of complex impulse responses h(q,n), with corresponding time delays $\tau(q) = q/fs$ and instants $t(n) = nT$. In this case, fs is the sampling frequency and T is the repetition period of the probing signal.

It should be noted that the probing signal used affects the simulations. For example, the duration of the probing signal pulse determines the maximum delay spread, while its reciprocal determines Doppler spread. Another important parameter is the probing signal band, which fixes the transmission band that can be simulated. In fact, if the user signal band exceeds the probing signal band, the exceeded band of the user's signal will be strongly attenuated.

As for the doppler effect, Watermark removes any mean Doppler shift V_0 from the sounding data before the channel estimation. This is done by resampling the raw acoustic data by a resampling factor $(1 - d)$, where $c = 1500m/s$ is the nominal sound speed and $d = V_0/c$. By convention, a positive velocity corresponds to a time dilation of the signal (i.e. positive range). Doppler effect elimination from the sounding data serves to minimize the measurement errors of the channel sounder. In this way, instantaneous Doppler spreading and time variant delay shifts around

the mean value are reproduced in direct replay. However, in order to transfer onto the input signal x(t) all Doppler effects experienced by the channel probing signal in the real channel, the mean shift is reinstalled before putting out the simulated packets.

4.3 Test bed LOON

The LOON (Littoral Ocean Observatory Network) is a permanent test bed implemented by the NATO STO Centre for Maritime Research and Experimentation (CMRE) that consists of both acoustic communication equipment as well as oceanographic and meteorological non-acoustic sensors. Typically, the acoustic communication equipment, which allows the transmission and reception of acoustic signals, is mounted on 1 m high tripods placed on the seabed, while non-acoustic sensors, used to measure environmental data over a long period of time (from hourly to seasonal), are positioned both in water and on land. Overall, this type of infrastructure emulates a real multi-asset scenario in which a wide range of experimental tests (from protocol to communication performance testing) can be performed to exploit different links. Furthermore, the possibility of collecting real environmental data allows for a correlation between the experimental results and the acoustic channel conditions. Over time, as reported in [20], several LOON deployments have been made by CMRE in different sites and with different equipment. In the following, we will limit ourselves to describing the 2020/2021 LOON version deployed in the Gulf of La Spezia (Italy), since that is the one of interest for this thesis work.

The usage of the 2020/2021 LOON version has been offered by CMRE to all interested universities, research centers, and companies (as WSENSE S.R.L.) selected during the TNA (Trans-national access) calls. As reported in [21], the test bed was composed of four bottom-mounted tripods (M1, M2, M3 and M4), a thermistor chain and a weather station with automated data acquisition of rain rate, wind speed and wind direction. As shown in figure 4.6b, tripods were placed at different relative distances on the seabed (about 11 m deep) and fitted with different acoustic capabilities based on the Woods Hole Micro-Modem, EvoLogics S2C 18/34 and arbitrary waveform transmission and recording capability (above 6 kHz). All

	M1	M2	M3	M4
M1	-	~660m	~310m	~480m
M2	~660m	-	~460m	~280m
M3	~310m	~460m	-	~200m
M4	~480m	~280m	~200m	-

(a) Distances between underwater tripods [21].

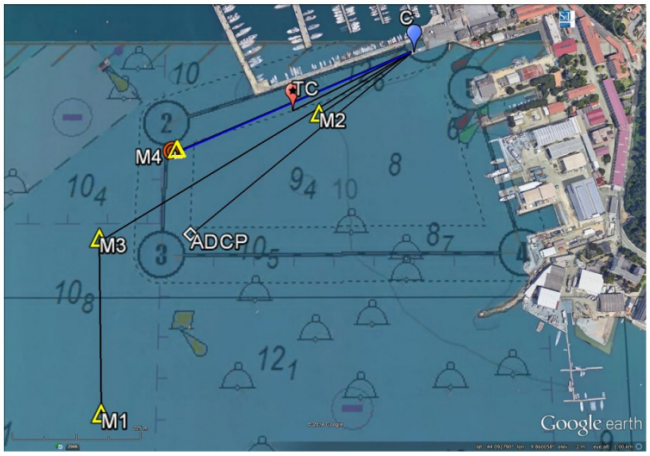

(b) LOON: location and deployed assets [21].

four tripods could be used for arbitrary waveform transmission, while only M1, M2, and M3 could be used for arbitrary waveform recording. This configuration allowed transmission and reception/recording of an acoustic signal through different communication links whose distances are summarized in table 4.6a. Thermistor chain, composed of ten sensors with a spacing of 1 m and placed from 1 m below the sea surface to the sea bottom, was adopted to continuously measuring the water column temperature. The sound speed was instead measured in only two points of the column water (at about 3 m and 10.5 m from the surface). In order to carry out the experimental transmissions through the LOON test bed, it was necessary to generate the signals to be transmitted in audio format. These signals had to meet the specifications (e.g. sample rate, center frequency, bandwidth, etc.) of the equipment that would be used for the transmission of the acoustic signals in the water. Regarding the transmission and reception of arbitrary waveforms, the Lubell LL916 system and the Ocean Sonics icListen Smart Hydrophone were used respectively [21]. The transmission source level could be set up to a maximum of 184 dB re 1μPa @ 1m before transmission but could no longer be changed during transmission. Acoustic signals could only be transmitted within the frequency band between 8 kHz and 14 kHz and at sampling frequencies of 44.1 kHz or 48 kHz. Audio files could be created in three different formats (PCM, WAV or FLAC) and with two different bit depths (16-bit and 24-bit). Once generated, the signals were shared with the CMRE team,

which would take care of their transmission and reception in the testbed.

Chapter 5

Doppler Estimation and Correction in JANUS Communications

5.1 Doppler estimation and correction methods

In the literature, several methods have been designed to estimate and compensate for Doppler effects in underwater communications. Many of the proposed algorithms perform single or multiple correlation processes on known signals attached to the transmitted sequence to extract the doppler estimation in terms of the compression/dilatation factor as well as a frequency shift. For example, in [22] the Doppler-induced time scaling distortion is estimated by applying a known waveform before and after the data packet so that, by correlating the received packet with a copy of the known waveform, the data packet duration can be obtained by measuring the time interval between the two correlation peeks. Furthermore, to minimize possible errors due to multipath copies of the transmission, a highly Doppler-tolerant waveform such as a linear or log frequency-modulated signal is used. In [8], single correlation is applied to a zeropadded (ZP) OFDM modulation (i.e. a multi-carrier system). In this case, a preamble and a postamble surround the whole ZP-OFDM packet, which consists of multiple OFDM symbols. As a first step, the scaling factor is again estimated by measuring the time duration between the preamble and

postamble signals around the packet and a resampling is applied to compensate for the coarse Doppler shift. Then, a fine compensation is carried out on each OFDM symbol to eliminate the residual Doppler shift. In [23], Zappa et al. estimate the Doppler dilatation factor by applying a Fourier analysis to three wakeup tones (preceding the JANUS packet). In [24] Doppler shift estimation is accomplished using the CAF method on a preamble (a known training sequence) prefixed to the data. The obtained Doppler shift estimation is first used to shift the central frequency and a linear interpolation is then applied to correct the time scaling of the signal. Finally, a fine compensation is applied to remove residual Doppler effects and improve the performance of the coherent receiver considered in the paper. The work in [10] uses the CAF method in a multi-carrier OFDM system, where the pilot signals, periodically inserted in the OFDM symbol, are considered to compute the CAF. A multi-branch auto-correlation (MBA) technique is proposed in [2] for OFDM-like systems, also exploiting pilot signal transmissions, and the results are compared with the ones in [10] and with SBA. In the case of MBA, the Doppler effect is estimated using a single correlation on each sub-carrier (similarly to some of the aforementioned works). From the presented results, it is evident that the MBA and CAF algorithms provide comparable results, while the SBA performs poorly.

5.2 Doppler estimation

Doppler measurements are generally performed by adding particular waveforms to the signal to be transmitted. For example, m-sequences, linear-frequency-modulated (LFM) or hyperbolic-frequency modulated (HFM) waveforms could be added before the data symbols for evaluating the frequency distortion [24], both before and after the data frame to measure the time differences between arrivals (then converted to time compression factors [22]).

In this thesis work, we exploit the JANUS preamble, composed of an m-sequence of 32 pseudo-random symbols, to estimate and compensate for the Doppler effect without requiring any modification to the standard. To do this, we use the cross-ambiguity function (CAF) method. The CAF represents the output of a matched filter on an input signal that is shifted in terms of delay and frequency (Doppler

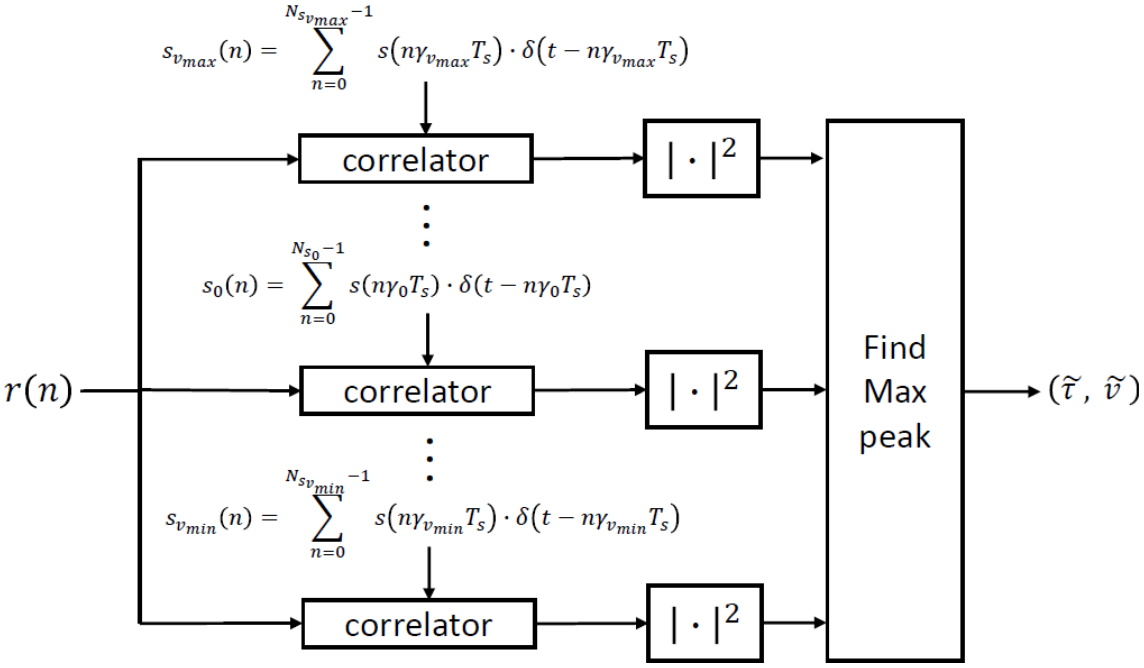

Figure 5.1: Block scheme for computing the CAF using a bank of correlators.

effect) [22], [25]. The mathematical expression that defines the CAF is dependent on the way the Doppler effect is modeled. Following the preceding references, the cross-ambiguity function for the narrowband model can be expressed as follows:

$$A_{narrowband}(\tau, f_D) = \int_{-\infty}^{+\infty} s(t)s^*(t+\tau)e^{j2\pi f_D t}dt \tag{5.1}$$

where $f_D = f_R - f_T = (\gamma - 1)f_T$ is the (fixed) frequency distortion and γ is the Doppler factor defined in equation (2.1). Instead, using the wideband model, we have:

$$A_{wideband}(\tau, \gamma) = \int_{-\infty}^{+\infty} s(\gamma t)s^*(t+\tau)dt \tag{5.2}$$

In both models, it can be easily seen that for $\gamma = 1$ the CAF is nothing but a simple auto-correlation of the signal. Instead, for $\gamma \neq 1$, the CAF consists in correlating the signal with a modified version of itself through the Doppler factor γ which, in the narrowband model, appears as a fixed frequency shift while, in the

wideband model, appears as a scale factor of time. In practice, the CAF can be computed by employing a bank of correlators, each of which is used to correlate the input signal with a Doppler-scaled replica of itself. This operation leads to a delay-Doppler scale grid in which the maximum of the CAF magnitude is searched. This operation leads to a delay-Doppler scale grid in which the maximum of the CAF magnitude is searched. More specifically, through the position of the peak of the CAF along the doppler scale, it is possible to extract the Doppler estimate, while, through the position of the peak of the CAF along the delay scale, it is possible to extract the time delay estimation, used for timing synchronization. Clearly, the receiver must know and compute in advance the Doppler-scaled replicas of the transmitted signal and the accuracy of the estimate will depend on the size of the correlator bank used. The number of correlators, as well as the scaled Doppler versions of the transmitted signal, depends on the expected range of the Doppler effect and the acceptable quantization error. Let M be the number of correlators and $s_0(t)$ the transmitted signal not distorted by Doppler effects. By sampling the signal at frequency f_s, we obtain:

$$s_0(n) = s_0(t) \cdot \sum_{n=0}^{N_{s_0}-1} \delta(t - nT_s) \tag{5.3}$$

where $T_s = 1/f_s$ is the sampling period and N_{s_0} is the number of samples required to cover the entire signal. Then, we can express the generic Doppler-scaled version $s_{v_i}(n)$ of the reference preamble as:

$$\begin{aligned} s_{v_i}(n) &= s_0(t) \cdot \sum_{n=0}^{Ns_{v_i}-1} \delta(t - n\gamma_{v_i}T_s) \\ &= \sum_{n=0}^{Ns_{v_i}-1} s_0(n\gamma_{v_i}T_s) \cdot \delta(t - n\gamma_{v_i}T_s) \end{aligned} \tag{5.4}$$

where the subscript v_i represents the relative speed of the signal affected by Doppler and Ns_{v_i} the number of samples of this same signal, which is equal to:

$$Ns_{v_i} = \frac{N_{s_0}}{\gamma_{v_i}} \qquad i = 0, \pm 1, ..., \pm\frac{M-1}{2} \tag{5.5}$$

To compute the CAF, the received signal $r(t)$ is sampled, converted to baseband and filtered to obtain $r(n)$. Then, $r(n)$ is correlated with all the Doppler-scaled

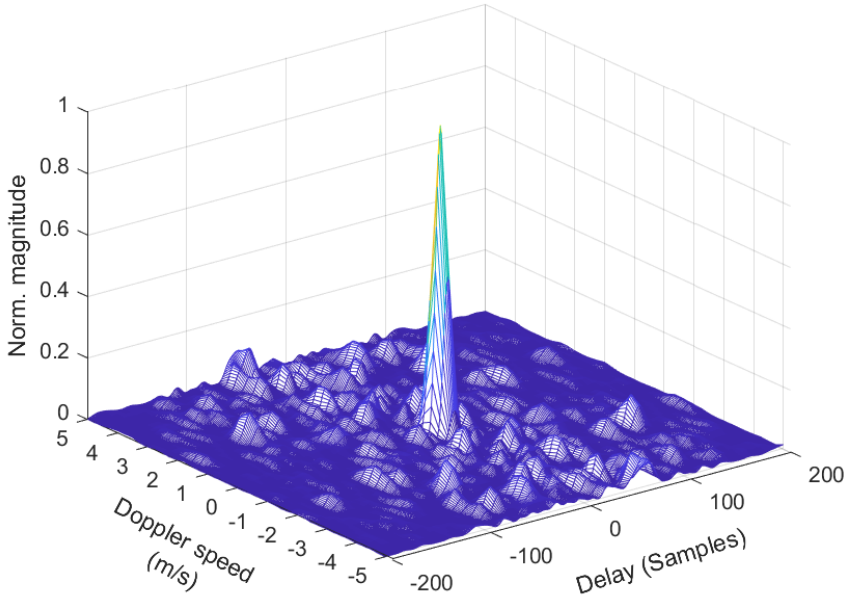

Figure 5.2: JANUS preamble CAF.

versions of the reference signal $s_0(n)$ as shown in figure 5.1. Finally, considering the squared module of each correlation, the CAF is obtained from the output of all the correlators.

Since in this work we are interested in the impact of relative motion between transmitter and receiver, we will express the Doppler range in terms of speed (measured in m/s) and we will estimate the Doppler scale factor via equation (2.1).

In this work, we apply the wideband CAF method to estimate and compensate the Doppler effect in JANUS acoustic communication, without requiring any modification to the standard. The proposed algorithm is implemented at the receiver, where the CAF method is applied: we use a bank of correlators in which the received signal is correlated with the known waveforms (the 32-chips of the JANUS preamble), prescaled by different Doppler scaling factors. Figure 5.2 shows the CAF of the JANUS preamble.

For this purpose, M doppler-scaled versions of the JANUS preamble must be generated, each of which corresponds to a different relative speed v_i between the transmitter and receiver. Without loss of generality, in this work, the CAF is de-

signed to estimate and correct distortions caused by relative movement up to $\pm 5m/s$ and with a resolution step of $\Delta v = 0.25m/s$. Thus, the total number of correlators M required is computed as the ratio between the speed range $[v_{min}, v_{max}]$ and the resolution plus 1:

$$M = \frac{v_{max} - v_{min}}{\Delta v} + 1 \tag{5.6}$$

while the relative speed v_i, corresponding to each correlator i is:

$$v_i = i \cdot \Delta v \qquad i = 0, \pm 1, ..., \pm \frac{M-1}{2} \tag{5.7}$$

The estimated Doppler will correspond to the highest value shown by the CAF, obtaining the relative speed $\hat{v}$. Although out of the scope of this work, the CAF peak may also be exploited to extract the time delay $\hat{\tau}$, used for time synchronization:

$$[\hat{v}, \hat{\tau}] = \arg\max_{v,\tau} |A(v, \tau)| \tag{5.8}$$

Since the CAF time and Doppler scales are quantized, searching for the CAF maximum value means finding the index of a matrix representing respectively the approximated values of the relative motion $\tilde{v}$ and the time delay $\tilde{\tau}$. Quadratic interpolation is then performed to improve the Doppler estimate.

5.3 Experimental results

We implemented the proposed technique in the WSense srl and Rome La Sapienza implementation of the JANUS STANAG standard modulation and then we tested the proposed mechanism both in simulation and in-field. For the simulations, we used the realistic underwater simulator Watermark described in section4.2 since it combines real channels and reproducible conditions. While in-field tests were conducted in the waters of the Italian harbor of La Spezia on two different circumstances. The first experimentation occurred during the 2nd JANUS Interoperability Fest 2019 [26], where the proposed Doppler estimation technique was tested in JANUS real-time transmission with the CMRE's unmanned surface vehicle (USV) towing one of the two modems. The second experimentation occurred some time later using the test bed LOON.

5.3.1 Watermark simulation

In our experiments, we used the NOF1 and NCS1 Watermark channels, which have a central frequency of 14 kHz (10-18 kHz band), the closest to JANUS standard (center frequency $fc = 11520$ Hz and band between $9440 - 13600$ Hz). Additionally, we shifted the JANUS signal to a center frequency of 14 kHz, sampled at 48 kHz, and we tested different relative speeds, from -5 to 5 m/s with steps of 1 m/s. We performed the tests by setting the size of the JANUS Cargo to 8, 16, 32 and 64 Bytes. Depending on the size of the Cargo, the packet transmission is repeated many times to fill the Watermark trace (almost 300 packets with an 8 Bytes Cargo). In the follow, we report the results obtained using a JANUS Cargo of 16 Bytes leading to about 130 packets transmission in the NOF1 channel and about 140 in the NCS1 channel.

For example, figure 5.3 shows the CAF obtained when the JANUS preamble is received through the Watermark NOF1 and NCS1 channels, with a simulated motion of 4 m/s. From the figure, the maximum of the CAF is clearly distinguishable from other minor peaks, despite the fact that the JANUS preamble is generally not used for this purpose. Note that the node's movement sums up with the watermark channel characteristics, which are summarized in Table 4.5 in terms of Delay spread and Doppler spread.

Figure 5.4 shows the results obtained on the Watermark NOF1 channel, with node' relative speeds of 2 and 4 m/s respectively. From the figure, it is clear that with our Doppler correction, almost all the packets are received without errors. Instead, without Doppler correction, the BER becomes quickly unacceptable, over 30% on average of bit errors per packet for speeds of 4 m/s. We repeated the same experiments using the Watermark NCS1 channel, which is the most challenging trace available. Figure 5.5 summarizes the results obtained in this scenario, with node motions of 2 and 4 m/s respectively. With the NCS1 trace, errors also appear when employing the proposed Doppler correction. Note, however, that packets received with a 50% bit errors indicate a possible detection or synchronization problem, rather than a Doppler distortion[1]. In any case, using our method, packets are correctly

[1]In these experiments, for simplicity, we employ a separated algorithm for packet detection before applying the CAF.

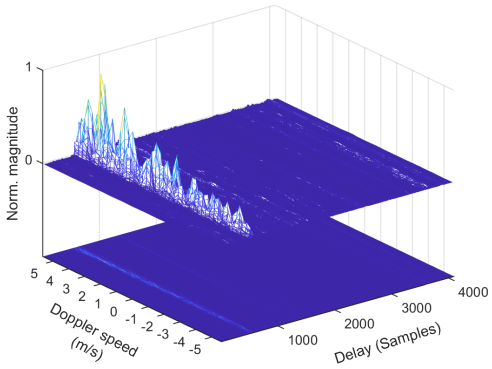

(a) NOF1: CAF

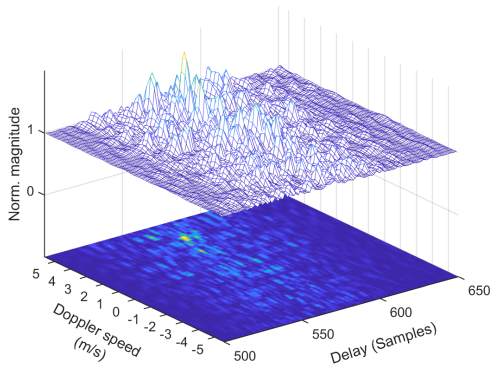

(b) NOF1: Details of CAF

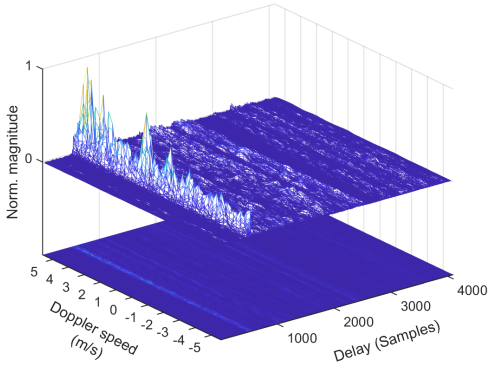

(c) NCS1: CAF

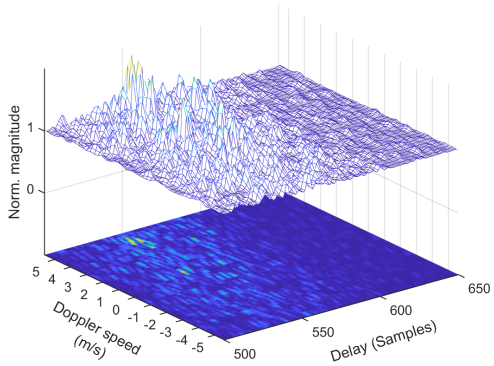

(d) NCS1: Details of CAF

Figure 5.3: Examples of CAF using the JANUS preamble. Watermark NOF1 and NCS1 channel, simulated motion 4 m/s.

received in over 90% of the cases, even at speeds of 4 m/s.

Figure 5.6 compares the results obtained on both channels in terms of BER when employing the proposed Doppler correction (solid line) or without it (dashed line). In the figure, each point represents the average bit errors per packet computed on the overall packets (about 130 for NOF1 and 140 for NCS1) obtained for each speed. As an example, at 2 m/s we can see the BER obtained from the bit errors of the packets shown in the figures 5.4(a) and 5.5(a). As already demonstrated in [23], JANUS is robust to Doppler speeds up to 2 m/s but above these relative speeds, the BER sharply increases on both the NOF1 and NCS1 channels. In these scenarios, a

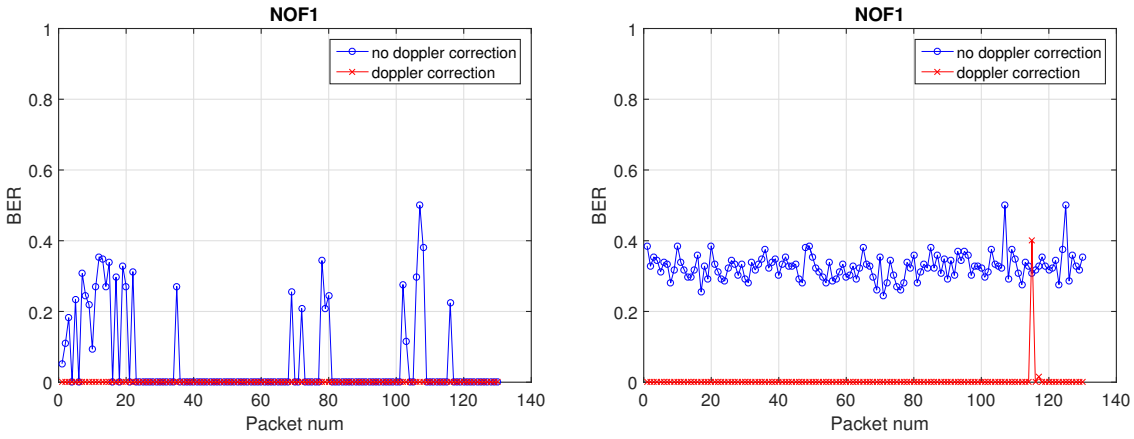

(a) 2 m/s (b) 4 m/s

Figure 5.4: Results obtained on Watermark NOF1 channel.

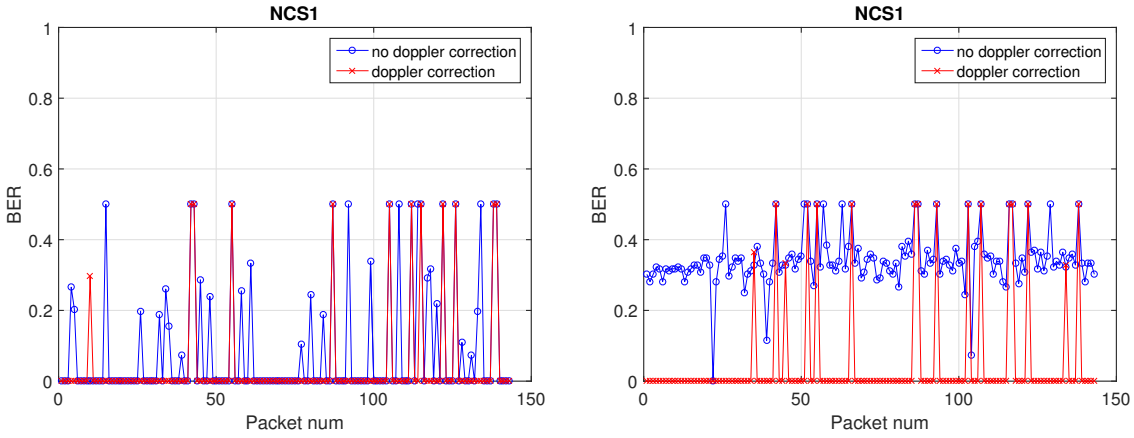

(a) 2 m/s (b) 4 m/s

Figure 5.5: Results obtained on Watermark NCS1 channel.

Doppler estimation and correction mechanism is required and the proposed method succeeds in this purpose, keeping the BER generally lower than 5%.

We also tested the performance obtained at different values of normalized signal-to-noise ratio (SNR), by adding AWGN noise to the Watermark traces (which are already affected by noise). We vary the E_b/N_0 SNR from 0 dB to 20dB, with steps of 2 dB, and tested the proposed method in the worst case scenario of 5 m/s speed. Figure 5.7 shows the results obtained with a 16 Bytes cargo on the NOF1 trace,

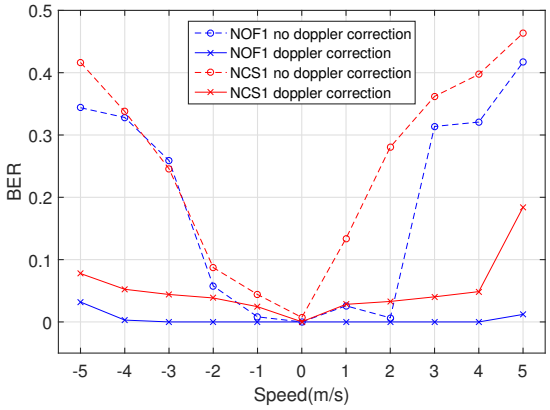

Figure 5.6: Average BER obtained with and without Doppler correction on NOF1 and NCS1 channels.

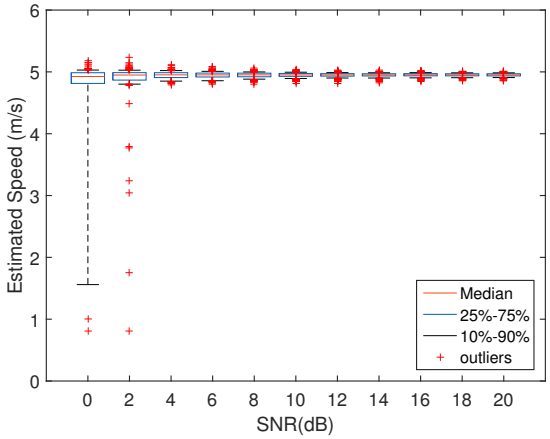

Figure 5.7: Estimated Doppler speed varying the SNR level.

from which it is clear that the proposed method successfully estimates the Doppler already with a SNR of 2 dB on top of the Watermark trace. Similar results were obtained on the NCS1 trace.

5.3.2 At sea results

The experiments were performed in the waters of the Italian harbor of La Spezia during the JANUS Interoperability Fest, an event organized by the Centre for Maritime Research and Experimentation (CMRE) in collaboration with the Italian Navy Naval Support and Experimentation Centre (CSSN), for allowing the guest compa-

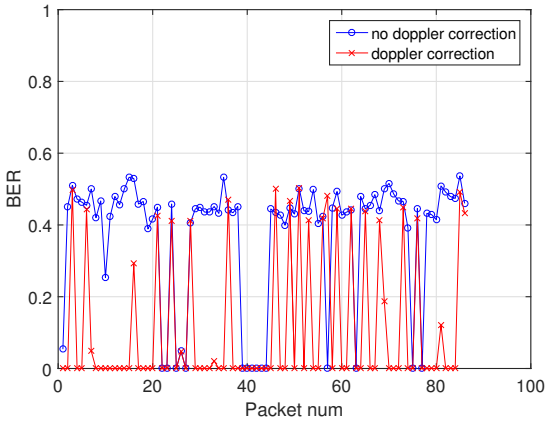

Figure 5.8: Results obtained in field using a USV.

nies (as WSENSE S.R.L.) to test their own JANUS implementation[2]. The setup was composed of a moving transmitter placed on a USV provided by CMRE and located about 200m away from the receiver that was instead stationary and dropped from the pier where water depth is about 10m. During these experiments, several JANUS packets with a size of 64 Bytes were transmitted from the USV moving at variable speeds spanning a range from -4 m/s to 4 m/s. Figure 5.8 shows the results obtained in this challenging scenario. Note that our implementation is designed to compensate for Doppler effects due to constant relative speeds, so large accelerations of the USV during the packet transmission might influence the results. Nevertheless, the proposed Doppler correction allows error-free reception in about 75% of the cases, with a BER of about 10%, while without Doppler correction the BER is 37% and only 16% of the packets were received without errors. In this last case, most of the error-free receptions are around the center of the experiment, when the USV spanning the -4m/s to 4m/s range crosses speeds around 0 m/s, i.e. no or slight Doppler effects that the robust JANUS modulation is able to tolerate.

[2]This work acknowledges the use of data that was made possible thanks to the Second JANUS Interoperability Fest, organized by CMRE with the support of CSSN.

5.3.3 LOON experimental campaign

An extensive experimental campaign was also conducted in the CMRE LOON test bed[3] described in section 4.3. This experimental campaign has been divided in two sessions. During both sessions, transmissions of JANUS signals were performed with different levels of Doppler distortions up to 5 m/s. In the first session all available transmission links between the tripods (M1, M2, M3 and M4) in the test bed were explored and the maximum source level was used. As opposed, during the second session, the experiments were performed only between the M3 and M4 tripods (i.e. the shortest link). In the latter case, different source levels (between 184 dB re 1 μ Pa @ 1m and 125 dB re 1 μ Pa @ 1m) were used in order to evaluate the performance of the proposed Doppler correction at the same distance but for different SNR levels. During the first session, we also performed several transmissions of probing signals in order to characterize the channel condition of this environment both in terms of time variability and acoustic propagation. This allowed us to correlate the channel conditions with the results of the experiments.

Channel sounding in the LOON testbed

In order to characterize the channel conditions in this scenario, we performed the channel sounding by transmitting probing signals for each possible communication link. To do this, we followed the approach used in [5], in which the probing signal was composed of trains of chirps transmitted without any pause between them. Indicating with $c_n = \exp(-j\pi(n - n^2/N_s))$ the chirp's samples sequence, the expression of the complex baseband probing signal is given in 5.3.3:

$$s(t) = \sum_{l=0}^{N_c} \sum_{n=0}^{N_s-1} c_n p(t - (n + lN_s)T_s)$$

where N_s is the number of samples used, N_c+1 is the number of repetitions of the chirp's samples sequence c_n, T_s is the signaling periods (i.e. the inverse of the channel bandwidth) and $p(t)$ is a root-raised-cosine signaling pulse. The complex baseband

[3]The authors would like to thank the NATO STO CMRE team for the excellent support during the experimental activity. The research is supported by the European Union's Horizon 2020 research and innovation programme under grant agreement No 731103.

probing signal in 5.3.3 was then translated to the central frequency ($11kHz$) of the LOON transducers used for transmissions.

Similar to Watermark probing signals, we transmitted trains composed of 258 consecutive chirps. Since the channel characteristics were not known in advance, we transmitted chirp trains with different chirp time durations of 64, 128 and 256 ms and with different root-raised-cosine filter lengths. The chirp pulse was transmitted with a bandwidth of 6 kHz in the range of 8-14kHz.

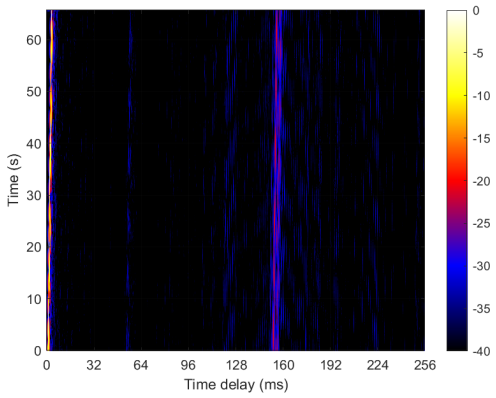

(a) channel impulse response

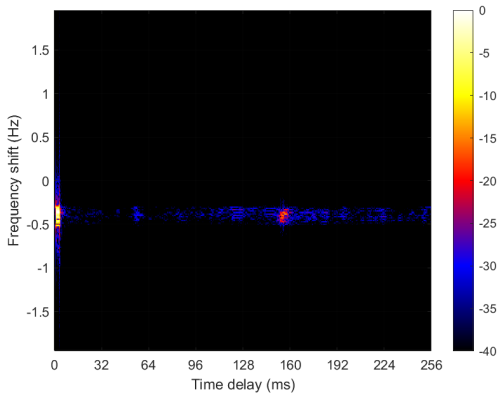

(b) Spreading function

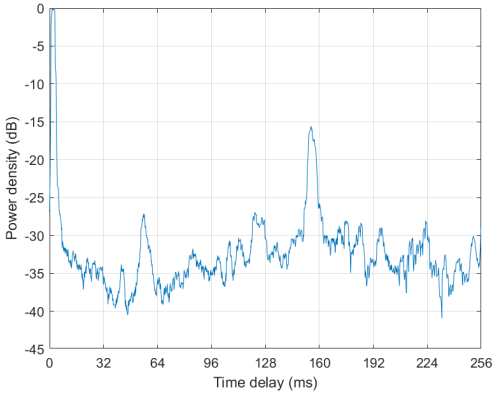

(c) Power delay profile

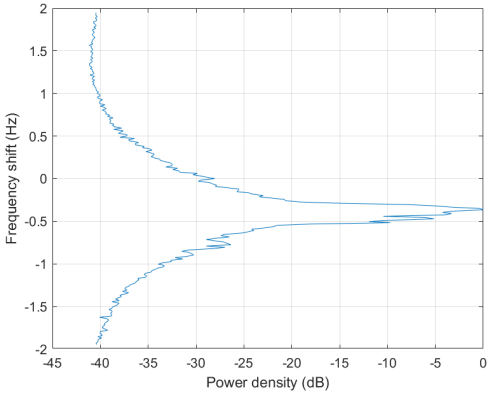

(d) Doppler spectrum

Figure 5.9: Link between M1(Receiver) and M2(Transmitter)

Once the transmissions were performed by the CMRE team and the recordings of the received signals were obtained, we then performed off-line the same approach used in [19] in order to obtain the impulse response matrix (i.e. the estimate of the

discrete time-varying channel impulse response). To do this, first we converted the recorded signal to complex baseband and downsampled it at a rate of $1/T_s$, then we applied a matched filter based on the complex baseband chirp. Finally, from the entire matched filter output, individual impulse responses were cropped and stacked in order to obtain a matrix of N_c complex impulse responses that is the estimate of the discrete version of the time-varying channel impulse response $h(t, \tau)$. Starting from the estimated $h(t, \tau)$, we computed the spreading function, the power delay profile and the Doppler power spectrum as defined in 2.3, 2.6 and 2.7.

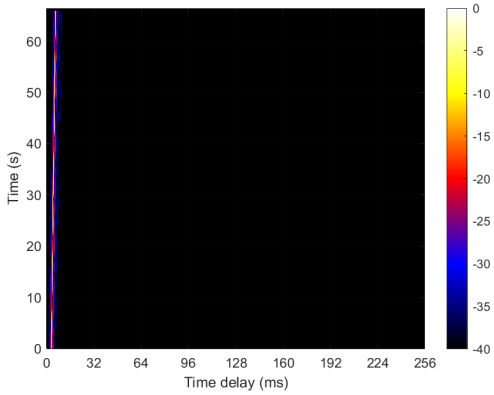

(a) channel impulse response

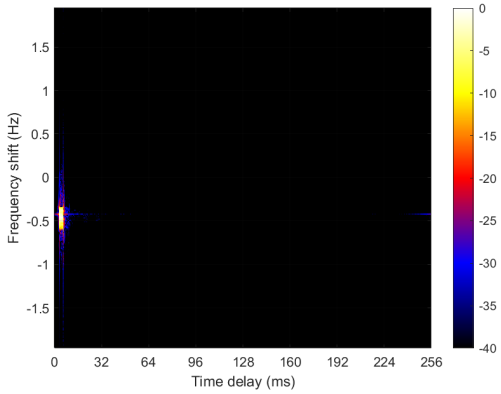

(b) Spreading function

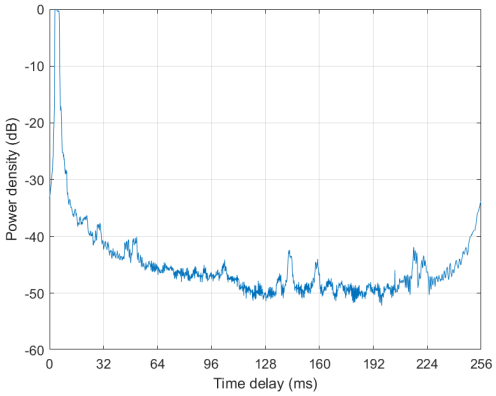

(c) Power delay profile

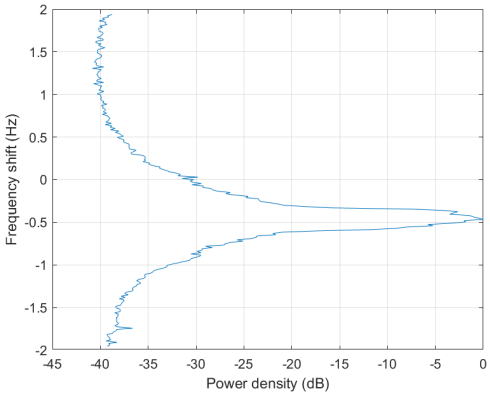

(d) Doppler spectrum

Figure 5.10: Link between M1(Receiver) and M3(Transmitter)

Analysis of these estimates revealed that the propagation structure changes from link to link. In fact, in addition to the main path, other propagation paths, due

to the bottom and sea surface reflections, can be observed. Depending on the link, these reflections may be more or less strong. As for the Doppler effect, we observed that a common frequency shift, between -0.3 Hz and -0.5 Hz, affects the Doppler spectrum of each link. Since the tripods are anchored to the bottom and therefore no intentional relative motion is present between transmitter and receiver, this common frequency shift is probably due to the clock frequency offsets of modem electronics. Furthermore, we observed that all links present a not very narrow peak in the Doppler spectrum, meaning that a certain Doppler spread is present in this environment.

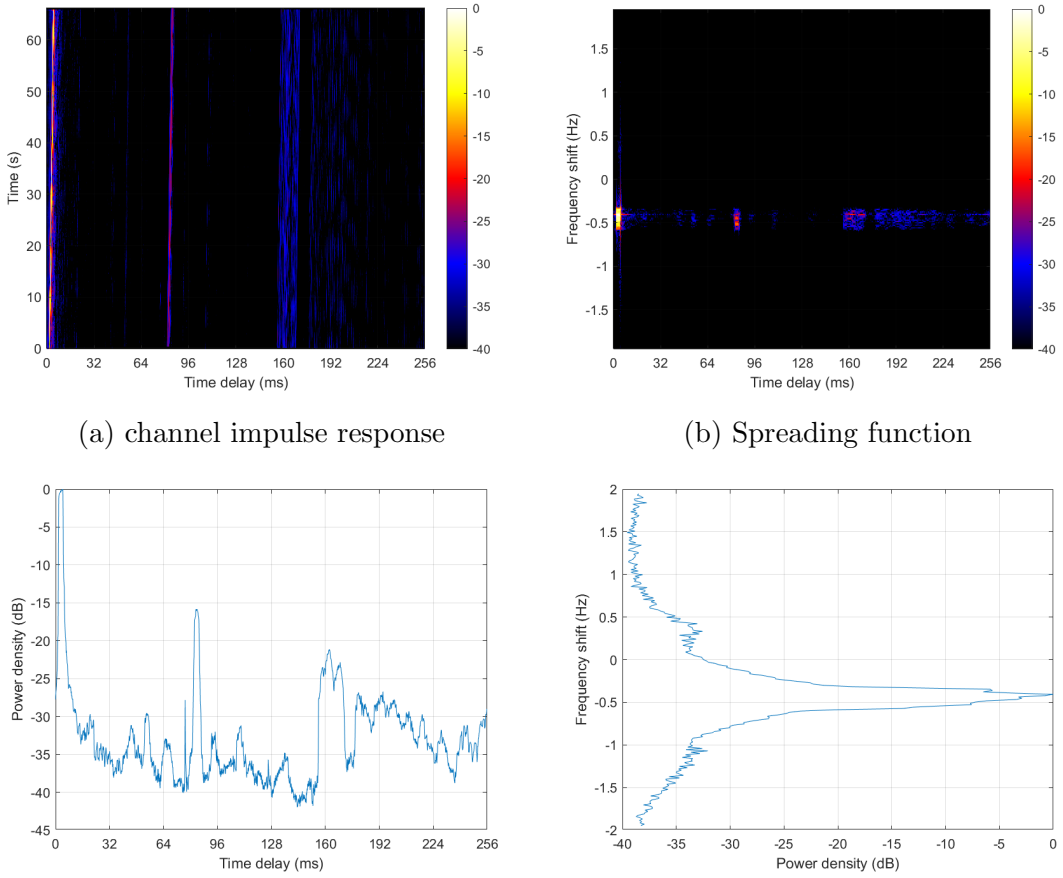

(a) channel impulse response

(b) Spreading function

(c) Power delay profile

(d) Doppler spectrum

Figure 5.11: Link between M1(Receiver) and M4(Transmitter)

For example, Figures from 5.9 to 5.11 show the estimates obtained in the specific

case in which the channel sounding was performed by using the M1 tripod as a receiver while the remaining tripods were used as transmitters one at a time. More specifically, the subfigures (a) and (b) of each group of figures represent the squared magnitude of the channel impulse response and the spreading function respectively, while the subfigures (c) and (d) represent the normalized power delay profile and the normalized Doppler spectrum respectively. By comparing the subfigures (a) of the Figures 5.9, 5.10 and 5.11, it is clear that the M1-M3 link is characterized by only one strong path, while in the M1-M2 and M1-M4 links, other different weak paths are present. In fact, the M1-M2 link is characterized by also a relatively weak cluster of paths at almost 160 ms preceded by two other more weak paths at almost 64 ms and 128 ms. From the power delay profile, it can be seen that the first two paths are about -27dB below the main path while the third path is -16dB below the main path. In the M1-M4 link, in addition to the main path, there is an evident path at about 80 ms (about -16dB below the main path in the power delay profile), and a more sparse cluster of paths around 160 ms as well as other more spare paths that start at about 176 ms and vanish at about 240 ms. In all three cases, it is possible to notice how the main path tends to lean towards the right, this behavior is caused by the clock-frequency offsets which, as already mentioned, affect all measures. The value of this frequency shift can be observed from the Doppler spectrum of each group of these Figures. Furthermore, by comparing the Doppler spectrum of each group of figures, it can be seen that, considering a power threshold of -20dB, the maximum Doppler shift is no more than 0.4 Hz.

First session

During the first session, all the tripods were used to transmit JANUS signals and this allowed for four transmission configurations, as summarized in table 5.1. In particular, for each configuration, one of the four tripods (between M1, M2, M3 and M4) was used for the transmission of the Janus signals, while the received signal was collected by all the remaining tripods (M1, M2 and M3) which allowed the storage of received waveforms. The goal of this first session was to test the reception of JANUS signals affected by Doppler distortions up to 5 m/s by evaluating the performances

in terms of PDR (Packet delivery ratio[4])

Config. ID	Transmitting tripod	Transmitted packets number	Link length (m)	Receiving tripod	Received packets number
1	M1	1680	~660	M2	1680
			~310	M3	1680
2	M2	1680	~660	M1	1680
			~460	M3	1680
3	M3	1680	~310	M1	1680
			~460	M2	1680
4	M4	1680	~480	M1	1680
			~280	M2	1680
			~200	M3	1680
		Total Transmitted packets 6720			**Total Received packets** 15120

Table 5.1: Experimental configuration for the first session of the LOON experimental campaign

In order to perform the aforementioned experimental transmissions, JANUS signals with Doppler distortions between -5 m/s and 5 m/s and digitally inserted at 0.5 m/s step were generated. Overall, a total of 21 Doppler speeds were simulated. For each of the 21 Doppler speeds, 20 packets with a cargo packet size of 8, 16, 32 and 64 Bytes were respectively generated. This means that from each of the four tripods up to 1680 Janus packets were transmitted.

The first experimental session took approximately 17 hours of continuous packet transmission, during which a total of 6720 packets were transmitted and a total of 15120 packets were recorded. The signals collected during the experimentation were analyzed off-line. The obtained results were reported in the table 5.2, where the PDR of both the baseline packets and the cargo ones were computed separately.

From table 5.2, it is possible to see that with the proposed Doppler correction,

[4]Packet delivery ratio was computed as the ratio of the number of packets successfully received to the total number of packets transmitted from the source

Transmitting tripods	Receiving tripod	Recorded packets number	Baseline packets PDR	Cargo packets PDR
M2	M1	1680	98,4%	98,3%
M3		1680	98,4%	98,3%
M4		1680	98,8%	98,6%
M1	M2	1680	98,2%	98,0%
M3		1680	93,2%	93,1%
M4		1680	97,0%	97,0%
M1	M3	1680	97,8%	97,6%
M2		1680	97,9%	97,7%
M4		1680	98,6%	98,2%

Table 5.2: PDR of the first experimental LOON session.

a PDR between 97% and 98% was obtained in almost all links. Only in one case, the PDR drop to 93%. The reason why PDR reached this value only in this isolated case is still being researched.

Using histogram graphs, Figures 5.12, 5.13 and 5.14 show in detail the PDRs related to the first macro-row of the table 5.2 (i.e. when M1 was used as a receiver, while M2, M3 and M4 were used to transmit JANUS packets). In particular, figure 5.12 shows the PDRs obtained when tripod M1 was used as the receiver and M2 as the transmitter. From this figure, it is possible to see that, in most cases, the 100% of the PDR was obtained. Cases in which the PDR deviates from 100% are scattered and isolated, and therefore most likely linked to unfavorable variations in channel conditions. The same considerations can be made by observing the figures 5.13 and 5.14 which show the PDRs of the other two links: link M1(receiver)-M3(transmitter) and link M1(receiver)-M4(transmitter) respectively. The PDR obtained when M2 and M3 were used for reception (i.e. rows 2 and 3 of the table 5.2), shows a similar behavior; therefore, for the sake of brevity, they will not be reported here.

Second session

In the second session, only tripods M3 and M4 were used to transmit JANUS signals. The goal of this second session was to test the reception of Doppler distorted JANUS

signals as the transmitted power level varies. In order to perform the aforementioned tests, JANUS signals were generated with Doppler distortion between -5 m/s and 5 m/s and digitally inserted at 1 m/s, for a total of 11 simulated Doppler speeds. For each of the 11 Doppler speeds, 40 packets with a long cargo packet size of 64 Bytes were generated. Transmission of these signals was performed at 7 different power levels. Specifically, transmissions were started at the maximum power level allowed by the transducer (184 dB re 1μPa @ 1m) and gradually lowered up to a power level of 125 dB re 1μ Pa @ 1m. The transmitted power levels, as well as the other experimental parameters, has been listed in table 5.3.

Cargo size (bytes)	Source power level (dB re 1µPa @ 1m)	Doppler speed (m/s)	Doppler speed step	Number of simulated Doppler speeds	Number of packets per speed	Number of transmitted packets
64	184	[-5, 5]	1 m/s	11	40	440
64	181	[-5, 5]	1 m/s	11	40	440
64	178	[-5, 5]	1 m/s	11	40	440
64	171	[-5, 5]	1 m/s	11	40	440
64	161	[-5, 5]	1 m/s	11	40	440
64	131	[-5, 5]	1 m/s	11	40	440
64	125	[-5, 5]	1 m/s	11	40	440
				Total transmitted packets		**3080**

Table 5.3: Experimental configuration for the second session of the LOON experimental campaign

The transmission of the signals described in the previous table was repeated twice and executed in two different days. As reported in table 5.4, during the second experimental session, a total of 6160 packets were transmitted and received.

The test configurations described in the previous table 5.3 were repeated two times, so a total of 6160 packets were transmitted and received. The test configurations, as well as the number of packets transmitted (both per single test and overall), are summarized in the following table.

All the signals collected during the experimentation were analyzed off-line in

Test day	Transmitting tripod	Receiving tripod	Number of transmitted packets
1th	M4	M3	3080
2nd	M4	M3	3080
			Total transmitted packets
			6160

Table 5.4: Experimental configuration for the second session of the LOON experimental campaign

Test round	Transmitting tripod	Receiving tripod	Number of transmitted packets	Baseline packets PDR	Cargo packets PDR
1°,2°	M4	M3	6160	86,41%	84,11%

Table 5.5: PDR of the entire second experimental LOON session.

terms of PDR for both baseline and cargo packets. Table 5.5 shows the overall PDR obtained by grouping the PDRs obtained during the first and second days of the second LOON experimental session. In line with what was expected, a degradation in performance was observed compared to the first experimentation session, where instead the power level was always the maximum available. Figure 5.15 shows more in detail the obtained PDR for a specific Doppler speed and source power level.

Anyway, table 5.5 shows the overall PDR obtained by grouping the PDRs obtained during the entire second LOON experimental session, while table 5.6 shows separately the PDR obtained during the first and second days. Also in this case, we considered JANUS signals with Doppler distortions between -5 m/s and 5 m/s at step 1 m/s and evaluated the performances in terms of PDR. A degradation of performance was observed, in line with what was expected.

Test round	Transmitting tripod	Receiving tripod	Number of transmitted packets	Baseline packets PDR	Cargo packets PDR
1°	M4	M3	3080	82,99%	79,25%
2°	M4	M3	3080	89,84%	88,96%

Table 5.6: PDR obtained during the first and second day of the second experimental LOON session.

(a) 8 bytes cargo

(b) 16 bytes cargo

(c) 32 bytes cargo

(d) 64 bytes cargo

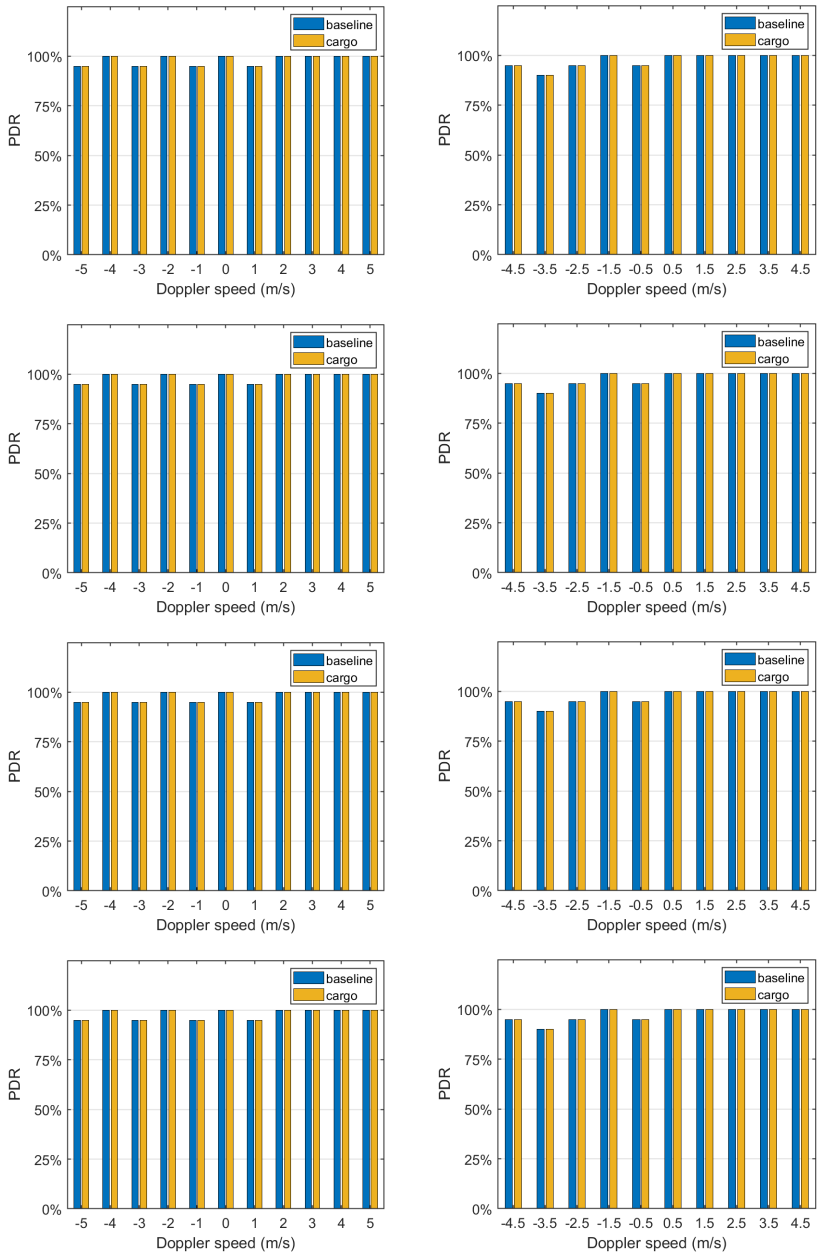

Figure 5.12: Case M1(receiver) - M2(transmitter). PDRs obtained considering JANUS packets with different cargo size and with doppler distortion between -5 m/s and 5 m/s at 0.5 m/s step.

(a) 8 bytes cargo

(b) 16 bytes cargo

(c) 32 bytes cargo

(d) 64 bytes cargo

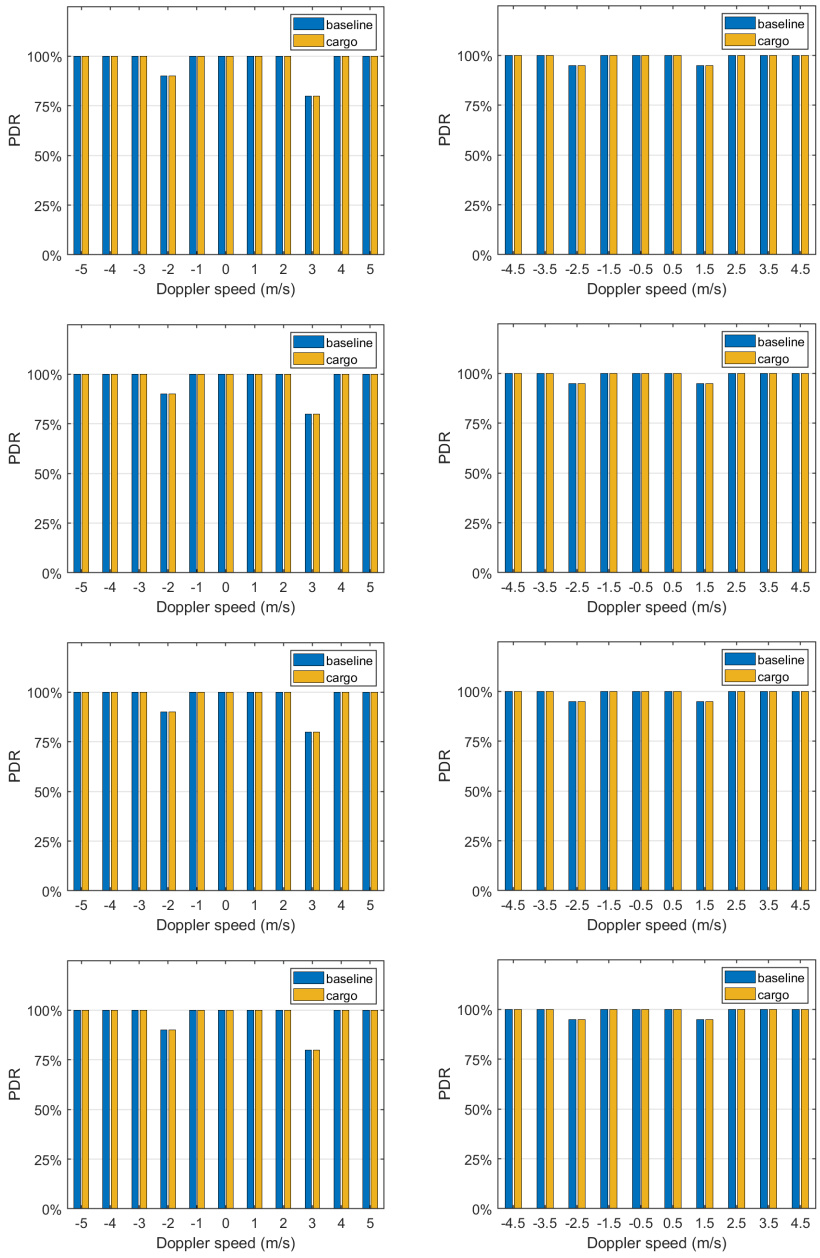

Figure 5.13: Case M1(receiver) - M3(transmitter). PDRs obtained considering JANUS packets with different cargo size and with doppler distortion between -5 m/s and 5 m/s at 0.5 m/s step.

(a) 8 bytes cargo

(b) 16 bytes cargo

(c) 32 bytes cargo

(d) 64 bytes cargo

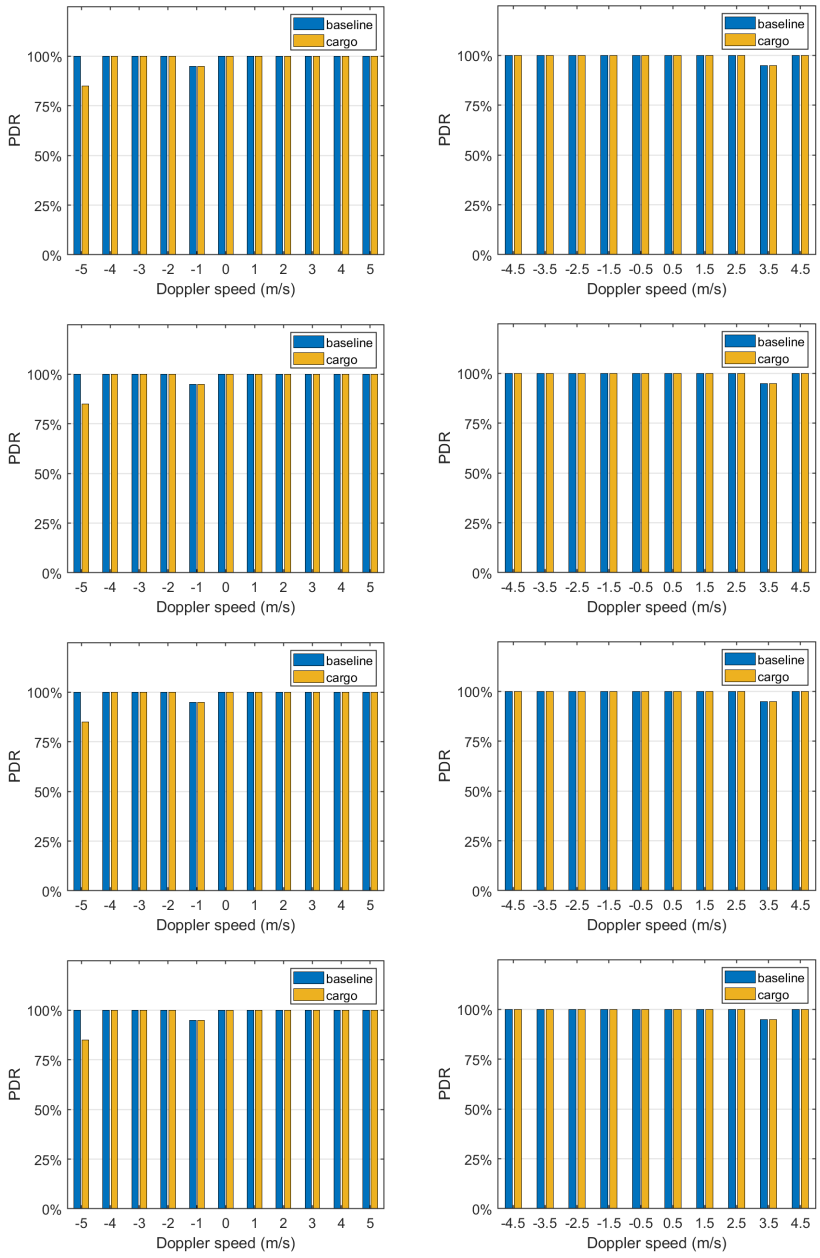

Figure 5.14: Case M1(receiver) - M4(transmitter). PDRs obtained considering JANUS packets with different cargo size and with doppler distortion between -5 m/s and 5 m/s at 0.5 m/s step.

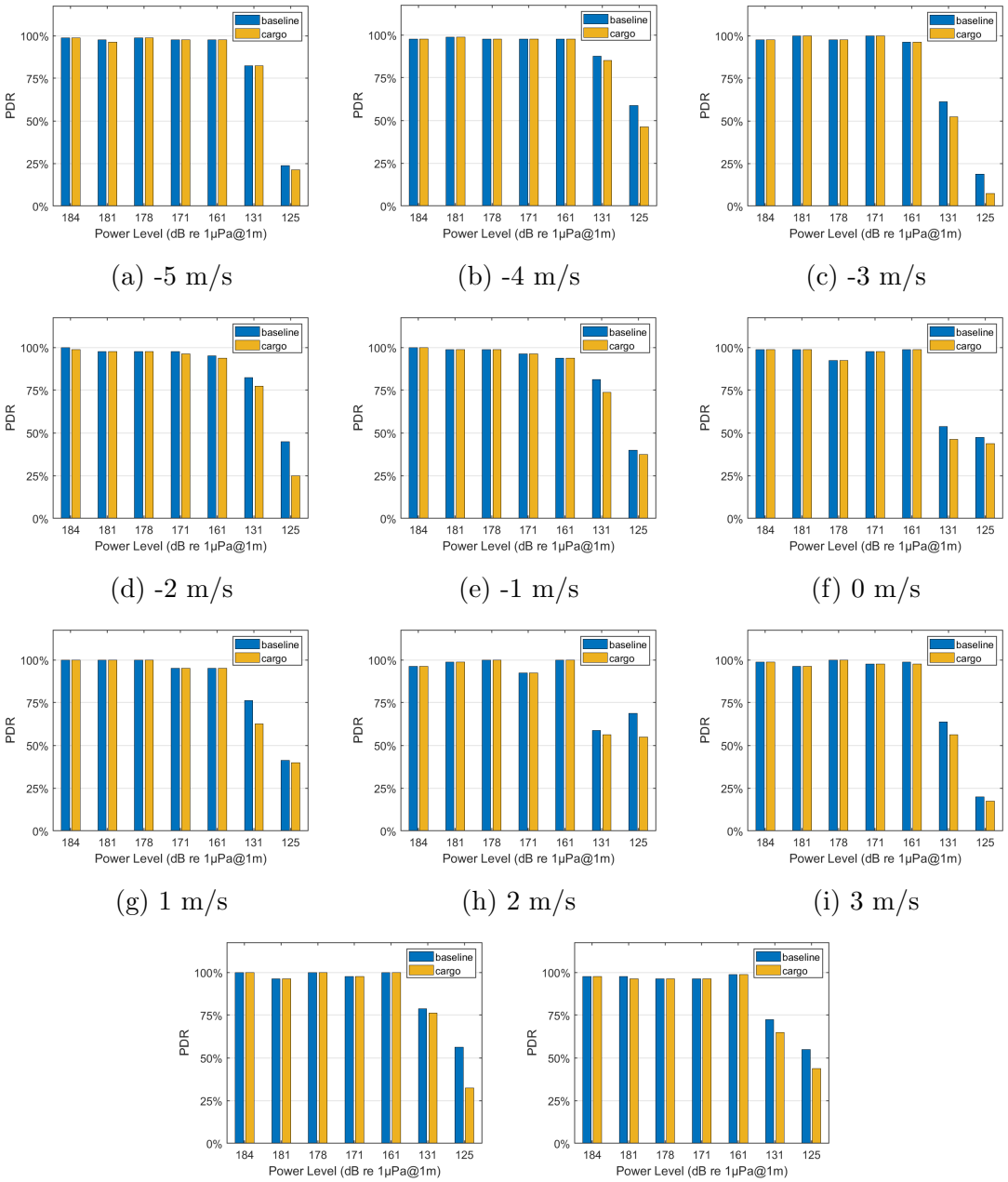

(a) -5 m/s (b) -4 m/s (c) -3 m/s

(d) -2 m/s (e) -1 m/s (f) 0 m/s

(g) 1 m/s (h) 2 m/s (i) 3 m/s

(j) 4 m/s (k) 5 m/s

Figure 5.15: PDRs obtained during the entire second LOON experimental session.

Chapter 6

S2C implementation overview

Since the S2C technique is proprietary and non-standard, we developed our own version of this modulation in MATLAB, following the typical structure of current S2C implementations [13]. However, unlike the latter, in our implementation, the transmitted frame is constituted by a preamble followed by a data packet, as shown in figure 6.1. The preamble is used for detection, synchronization and Doppler estimation purposes, while the data packet is used to carry out binary information.

Figure 6.1: S2C packet frame

The advantage of using this type of frame structure (e.g. rather than the one used in [13]) lies in the ability to perform real-time receiving processing. Indeed, in [13], where a preamble and a postamble are placed before and after the data and used for doppler estimation purposes, packet elaboration can start only after the whole data is received. In real-time applications, where latency has a relevant impact on the performance of communication systems, elimination of this processing delay could have a not negligible benefit.

Figure 6.2 shows the block diagram of our S2C transmitter. The first block

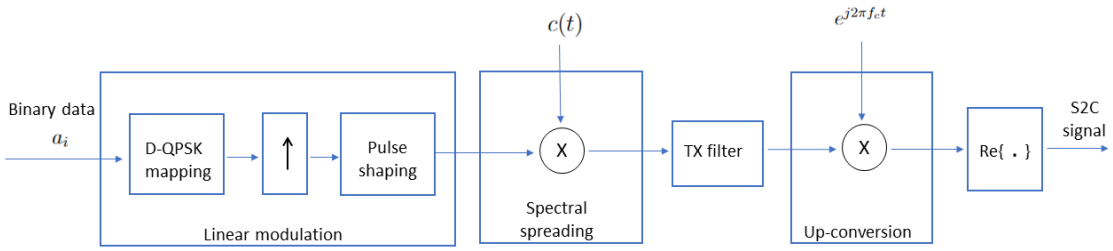

Figure 6.2: S2C transmitter

is constituted by a conventional linear modulator in which binary information is mapped into complex D-QPSK symbols. The obtained complex symbol sequence is first up-sampled and then passed through the shaping filter in order to form the baseband modulated D-QPSK signal. At this stage, the continuous time version of the base band signal can be expressed as in 6.1:

$$s(t) = \sum_{i=0}^{N_{symb}-1} a_i g(t - iT) \tag{6.1}$$

where a_i represents the complex D-QPSK sequence of N_{symb} symbols, T the D-QPSK symbol duration, and g(t) the pulse shaping filter function. If a root-raised-cosine pulse with roll-off factor α is used, as in our case, the symbol bandwidth B is given by $B \approx \frac{1+\alpha}{T}$.

Once we have the modulating signal, we perform the spreading operation in the second block of the diagram with a simple multiplication by the baseband sweep-spread carrier. In this case, the sweep-spread carrier $c(t)_{BB}$ is defined in its base band form as in 6.2:

$$c(t)_{BB} = \exp\{j(\pi B_{sw}\phi(t) - k\phi(t))\} \tag{6.2}$$

where $B_{SW} = f_H - f_L$ is the sweep bandwidth while $\phi(t)$ is the saw-tooth periodic sweep function, with period T_{SW} as defined in 6.3:

$$\phi(t) = t - \left\lfloor \frac{t}{T_{SW}} \right\rfloor T_{SW} \tag{6.3}$$

The sweep bandwidth and the sweep duration defined above determine the slope sweep as in 3.3 and since the latter affects the S2C receiver's ability to resolve echo arrivals (i.e. the multipath channel structure), its value is a project-specific parameter. However, the slope value is typically taken to be an integer multiple of the symbol spacing. In our case, we follow this specification, so the number M_{symb} of D-QPSK symbols coded on a single sweep is given by $M_{symb} = \lfloor T_{\text{sw}}/T \rfloor$. Clearly, using a D-QPSK, the resulting Channel Bit rate is given by $R = \frac{2M_{symb}}{T_{\text{sw}}}$ while the packet duration depends on the amount of binary data to be transmitted. The optimal duration of the data packet as well as the quantity of data transmitted per packet are not the subject of this work.

The last three blocks are used to transform the complex S2C baseband signal into one suitable for transmission on the underwater channel (i.e. the real passband signal). Therefor, the complex S2C base band signal is first passed through a transmission filter, then is up-converted at the central frequency f_c and finally the real part is taken. The real pass band S2C signal can be expressed as in 6.4:

$$x(t) = \text{Re}\left\{(s(t)c_{BB}(t)) * h_{TX}(t)e^{j2\pi f_c t}\right\} \tag{6.4}$$

where the "*" operand represents the convolution operation while $h_{TX}(t)$ represents the filter transmission filter used also on the received side.

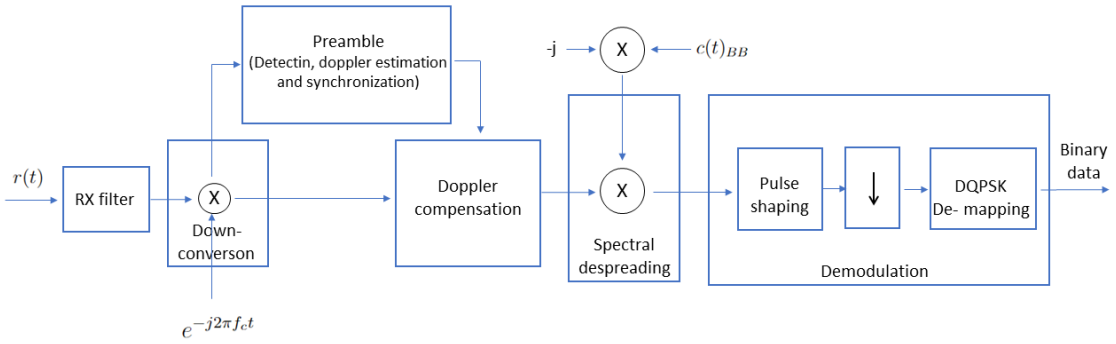

Figure 6.3: S2C receiver

Figure 6.3 shows the block diagram of the S2C receiver. As shown in this fig-

ure, when the S2C signal is received, it is filtered and downconverted to baseband. Now, the complex base band S2C signal passes through the preamble block and doppler compensation block. The first is used to operate detection and extract the time (synchronization) and doppler estimation, while the second block performs the appropriate compensation based on the estimated value. These two blocks will be better described below. Subsequently, the despreading operation is applied to the compensated baseband S2C signal, multiplying the latter by the sweep-spread carrier with an inverse slope. Finally, the last block performs the conventional demodulation operation to obtain the binary data.

6.1 Doppler compensation for S2C modulation

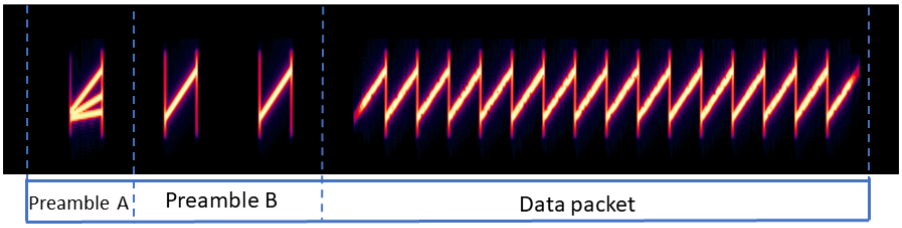

Figure 6.4: S2C frame

As anticipated in section 3.2 the transmitted frame is constituted by a preamble followed by data symbols, where the preamble is used for detection, synchronization and Doppler estimation purposes. In our implementation, we perform the last step in two steps by performing a coarse and a fine estimate. Figure 6.4 shows the spectrogram of our S2C signal as well as the transmitted frame in detail. From this figure, it can be seen that the preamble contains two types of waveforms: i) a first symbol composed of three overlapped chirps with different slopes; ii) two linear unmodulated chirps. The first waveform (Preamble-A) is used to perform both signal detection and coarse timing and Doppler estimation and this task is accomplished by applying the cross-ambiguity function (CAF) method likewise as described in 5.2. Therefore, also in this case, we use a bank of correlators, where each branch

matches with a particular doppler distortion. An S2C packet will be detected if a correlation metric greater than a certain threshold value is obtained from any of the correlator branches. If a detection occurs, the coarse Doppler scale estimate and synchronization point are also obtained from the branch that detected the largest correlation metric. Figure 6.5 shows that the Preamble A autocorrelation has a

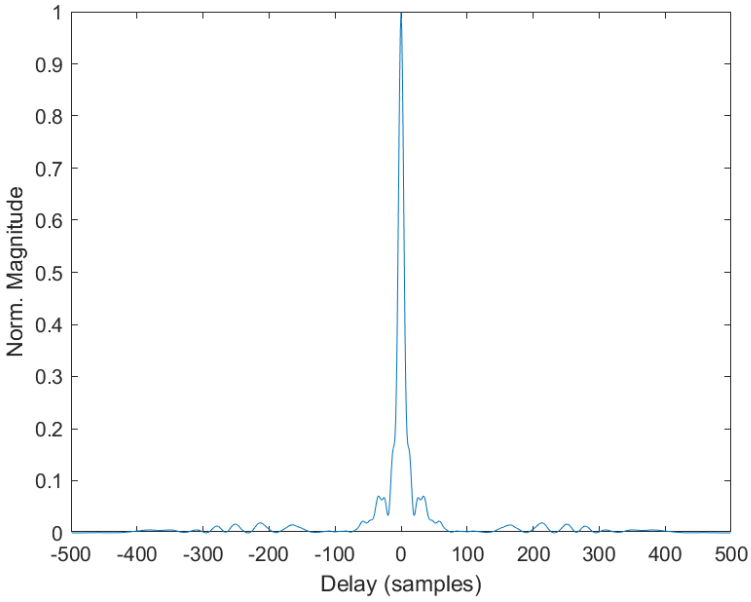

Figure 6.5: Preamble-A autocorrelation

sharp peak. This feature makes this waveform suitable for time detection purposes.

Although the application of the CAF method described above follows the same procedure used to perform the estimation and compensation of the Doppler effect in JANUS communications (section 5), the use of the extracted estimates (both in time and in frequency) is different. In the case of S2C, the Doppler factor estimated in this initial phase is not applied to the rest of the received signal but is estimated several times during the reception process to obtain a more accurate and updated estimate. This fine estimate is necessary because, unlike the FH-based modulation schemes (like JANUS), which are less sensitive to small Doppler variations, S2C modulation is much more sensitive to Doppler shift errors for reasons that will be better explained below.

The second waveform, referred to as "Preamble-B", is used to initiate the aforementioned fine Doppler estimation, which eliminates residual Doppler and timing errors. To do this, we use a self-autocorrelation method similar to that used in OFDM communication systems that adopt the cyclic prefix (CP) [27]. In OFDM systems, the cyclic prefix is constructed by adding at the beginning of an OFDM symbol a copy of the last part of the symbol itself. On the receiver side, the signal that is acquired gradually is cross-correlated with itself. When the initial part of the OFDM symbol (i.e. the CP) coincides with the last part of the OFDM symbol, the correlation peak increases and the OFDM symbol is located. One of the advantages of this method is that any unknown expansion/compression of the waveform affects both sides equally, as long as a constant variation during the OFDM symbol can be assumed.

In our case, we use this method to cross-correlate the two linear unmodulated chirps. More specifically, by using the first coarse time estimation, we roughly identify the position of the two up-chirps and then, through a sliding correlation window, we perform the cross-correlation between the two received waveforms. If no doppler expansion or compression occurs, the cross-correlation will be located at zero delay, otherwise a delay will be detected and the doppler factor will be calculated. Through this fine doppler factor estimate, we compute the starting instant of the data packet. It is clear that the validity of this method is suited to all the cases in which the doppler factor can be assumed to be constant, at least in this interval duration. However, assuming that the assumption is satisfied for preamble-B, it is not necessarily also satisfied for the data packet that has a longer duration. Effectively, rapid changes in the Doppler factor are very likely to occur in a dynamic channel such as the underwater one. To this reason, in our implementation, we also adopt a Doppler tracking procedure to follow any expansion or compression of the waveform. To track these changes, we insert a pilot symbol among the data symbols. Although this operation reduces the symbol rate, its application is important in order to reduce the timing error. In fact, if any expansion or compression of the signal occurs, the correct symbol sampling instant would shift in time accordingly. Figure 6.6 shows in detail the functioning of the Doppler compensation block of the schematic S2C receiver (figure 6.3) that performs the doppler tracking. The process starts when the Preamble-B processing is ended and the starting instant of

the data packet to be demodulated as well as the first doppler fine estimation are known. The latter is used to resample the reference pilot symbol to find the known pilot symbol added along the data packet before its transmission. The pilot symbol search is performed through a correlation process between the resampled reference pilot symbol and the data packet. When the received pilot symbol is located, a new doppler factor is computed and used to resample the part of the received signal to be demodulated. It should be noted that the estimated doppler factor is used both to compensate for any expansion or compression of the waveform as well as any residual CFO (carrier frequency offset), whether the latter is caused by an actual relative movement between the transmitter and receiver or by a frequency mismatch in the transmitter and receiver oscillators. The process described above is recursively performed until the data packet is finished.

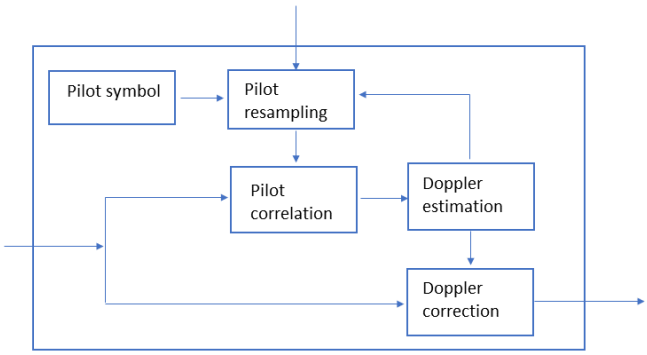

Figure 6.6: S2C Doppler tracking block diagram

6.2 Simulation environment

To evaluate the performance of our S2C implementation, we conducted several software simulations using Bellhop [15], a ray tracing software for modeling acoustic propagation in underwater environments. In order to evaluate the general behavior of our implementation in different conditions, we considered different underwater scenarios by varying the bottom depth, the reception range and the transmitter/receiver depth (for simplicity, both the transmitter and receiver are placed at the

same depth). Unless otherwise specified, the parameters used in our simulations are summarized in table 6.1. Since we were interested in evaluating the performance of our S2C implementation for shallow water applications with strong multipath, we consider a bottom depth between 10 m and 200 m and a transmitter/receiver depth in the range [2-120] m. Distortions due to Doppler effects were also included in our simulations by considering transceiver relative motions up to 5 m/s both in approaching and departing directions (we also tested relative headings of 90° and 45°). Regarding the modulation parameters, we considered the 18-34 kHz frequency band, a differential QPSK modulation scheme and a fixed packet length of 16 sweeps for all simulations. Instead, we vary the sweep duration (2 ms and 4 ms) and the number of coded symbols per sweep (between 1 and 10). For each combination of parameters, a Bellhop simulation was run and the symbol error rate was extracted (for simplicity, we consider a constant sound speed profile of 1500 m/s and neglect ambient noise). In total, almost 400,000 different experiments were executed and, for the sake of brevity, only a subset of the obtained results will be shown. Moreover, to provide a global picture of the performance obtained in a specific environment, we do not provide detailed results for each S2C parameter tested, but we summarize all the results obtained in terms of the empirical Cumulative Distribution Function (CDF) of the symbol error rate. In other words, the CDF will depict the fraction of simulated scenarios where errors are lower than a certain threshold. Finally, in order to track also undetected packets, the CDF plots incorporate these events, considering these packets with an "undefined" symbol error value. Thus, if undetected packets are present, at the top of the CDF graph, the curve will not reach unity and this gap quantifies the number of missed packets. This allows us to visualize the percentage of undetected packets, if any, together with the detected packets, as will be clear in the next section.

6.2.1 Numerical results

Among the obtained results, we focus on the impact of the depth, the symbols' length (also separating sweep duration and number of symbols per sweep) and Doppler effects. As a first result, we observe that the performance of our S2C implementation improves as the depth of the seabed increases, regardless of all the other parameters

Table 6.1: Simulation parameters.

Parameter	Value
Sound speed profile (m/s)	1500
Bottom depth (m)	5, 10, 20, 60, 120, 200
Transceivers' depth (m)	2, 5, 20, 60, 80, 100
Receiver distance (m)	100, 500, 1000, 1500, 2000, 3000
Receiver direction (deg)	0°, 90°, 45°
Receiver speed (m/s)	[-5, 5] in steps of 1 m/s
Frequency band (kHz)	18–34
Packet length (sweeps)	16
Sweep duration (ms)	2, 4
Modulation	DQPSK
Symbols per sweep	1, 2, 4, 8, 10

(e.g. receiver speed, number of coded symbols per sweep, etc.). This can be visualized in Figure 6.7 which shows the CDF of the symbol errors obtained with bottom depths of 10m, 120 m and 200 m, in a scenario constituted by a transmitter and receiver fixed at a depth of 2m and distant by 100 m from each other. Furthermore, in order to better understand the impact of the sweep duration, we separate in the figure the results obtained with sweeps of 2 ms (blue curve) and 4 ms (red curve). In general, figure 6.7 shows that the obtained symbol error is relatively high in shallow waters (i.e. with bottom depths of 10 m) regardless of the sweep duration, while for greater depths (i.e. 120 m and 200 m) over 80% of the symbols are received without errors. Note that, at the top of the CDF graphs, if undetected packets are present, the curve does not reach unity and this gap quantifies such missed packets. From the figure, it is clear that in almost all scenarios, packets with 4 ms of sweep duration are correctly detected (no gaps), while 2 ms sweeps are less robust with not synchronized packets in the range of 1-10% (the small gap between the right end of the blue curve and 1 on the y axis).

As for the impact of the symbols' length, intuitively an increase in the number of symbols per sweep leads to a possible increase in symbol errors. This behavior can be seen in figure 6.8a that shows the CDF obtained with bottom depth of 120 m

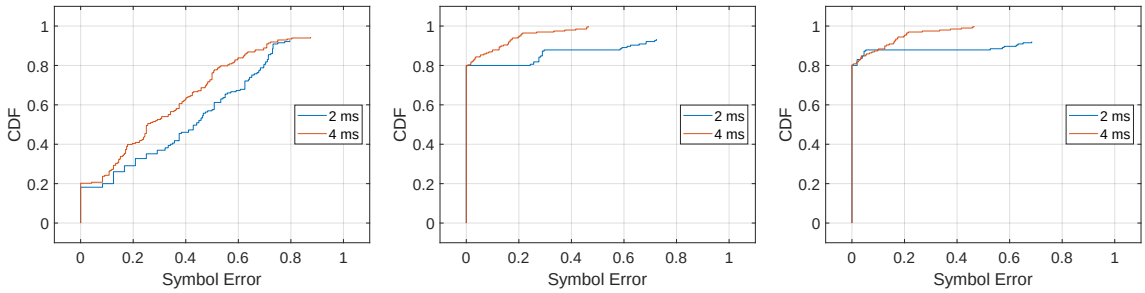

(a) 10 m bottom depth (b) 120 m bottom depth (c) 200 m bottom depth

Figure 6.7: CDF of the symbol errors as the bottom depth increases and considering both 2 ms and 4 ms of sweep durations. The depth of the transmitter and receiver is 2 m, and the range is 100 m.

and transceivers placed at depth of 5 m and distant 100 m away. Each curve in the CDF plots is related to packets with a specific number of coded symbols per sweep, regardless of the sweep duration and the transceivers' speed and direction. From the figure, it is clear that increasing the number of coded symbols per sweep produces an increase in the symbol error and that only 1 or 2 symbols can be transmitted in any condition with low errors. Instead, with a greater number of coded symbols per sweep (i.e. 4, 8 and 10) the percentage of packets received without error drops to around 20%. Considering separately the results obtained using 2 ms or 4 ms sweep duration, figure 6.8b shows that with 2 ms sweeps only packets with 1 or 2 symbols per sweep are received almost without errors, while the symbol error becomes unacceptable with a higher number of symbols per sweep. Instead, with 4 ms sweeps (figure 6.8c), in some cases even 10 symbols/sweep can be used without symbol error (about 40% of the scenarios considered).

In our simulations, we considered Doppler distortion caused by a departing/approaching receiver and simulated speeds in the range between -5 m/s and 5 m/s, in steps of 1 m/s. We also simulated headings of 0°, 90° and 45°. Figure 6.9 shows the CDF obtained for three specific transmitter/receiver distances: 500 m, 100 m, and 1500 m. From the figure, it is clear that, up to a distance of 500 m, Doppler

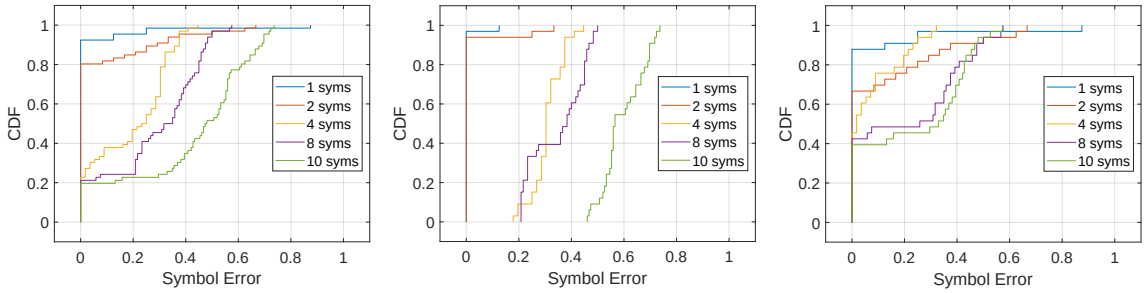

(a) 2 ms and 4 ms sweep duration

(b) 2 ms sweep duration

(c) 4 ms sweep duration

Figure 6.8: CDF of the symbol error rate with different number of symbols per sweep, 120 m of bottom depth, 5m transmitter/receiver depth and 100 m range.

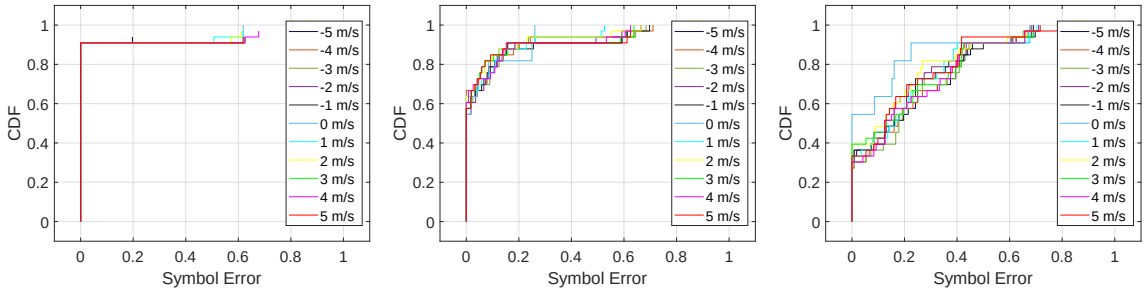

(a) Distance of 500 m.

(b) Distance of 1000 m.

(c) Distance of 1500 m.

Figure 6.9: Impact of Doppler effects on the symbol error rate (receiver moving in different directions). Bottom depth of 200 m and transmitter/receiver depth of 2 m.

distortions are correctly compensated independently of the extent of the Doppler distortion, with an error-free reception in over 90% of the scenarios. Instead, as the distance increases, the percentage of packets without error decreases as well, but the impact of Doppler is limited (results are almost independent of the Doppler distortion).

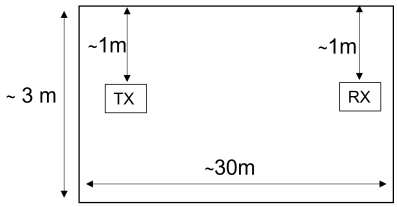

(a) Schematic experimental setup in the harbor of Santa Marinella, close to Rome, Italy.

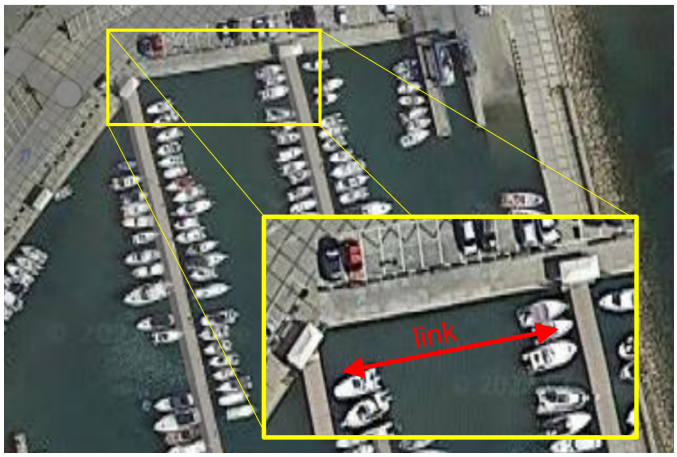

(b) Experimental setup in the small harbor of Santa Marinella, close to Rome, Italy.

6.3 At sea experiments

To test our S2C implementation in a real underwater environment, we conducted some experimental tests in the small harbor of Santa Marinella, close to Rome, Italy. As shown in figures 6.10b and figure 6.10a, the experimental setup was composed by a transmitter and receiver placed approximately 30 m apart and lowered from the pier to a depth of about 1 m, where the bottom depth was approximately 3 m. As transmitting and receiving nodes, we used two HS-Series Evologics underwater acoustic modems (HS-EVO) [28], piloted by personal computers. The HS-EVO modems were made available by the WSense srl company and were used in Software Defined Modem (SDM) mode to transmit and receive arbitrary waveforms. The transmission of the S2C waveforms was performed in the HS-EVO operating frequency band which ranges from 120 kHz to 180 kHz and with a sampling frequency of 500 kHz.

During the experimental S2C tests, both short (16 sweeps) and long (32 sweeps) packets were transmitted. For each of these packet lengths, up to eleven different S2C configurations were tested (i.e. different combinations of sweep duration and number of encoded symbols per sweep) and each experiment was executed ten times (for each configuration, 10 packets were transmitted). The specific configuration parameters employed during the tests are summarized in table 6.2. In particular,

Table 6.2: S2C configurations used in experiments at sea.

Sweep duration $[ms]$	Symbols per sweep $[\#]$	Spectral Efficiency $[b/s/Hz]$	Channel Rate $[b/s]$
2	1	0,017	1000
2	2	0,03	2000
2	4	0,067	4000
2	8	0,13	8000
2	10	0,16	10000
4	1	0,008	500
4	2	0,017	1000
4	4	0,03	2000
4	8	0,067	4000
4	10	0,08	5000

we transmitted S2C packets with both 2 ms and 4 ms of sweep duration and for each of them we encoded up to ten symbols per sweep. Table 6.2 also reports the spectral efficiency (column 2) and the raw data rate (column 3) related to each specific configuration. In our tests, no error-correcting code has been used, so the reported data rates are intended as simple upper bounds. It should be noted that, although the transducers should allow higher bit rates, the configuration parameters used were the only ones available at the time of experimentation. In the future, we plan to extend the configuration settings further.

In figure 6.11 an example of an S2C signal received during these experiments is shown. From this figure, the presence of multipath effects can be observed. Indeed, a second echo arrival coming from a different path than the main one is quite visible almost immediately after the beginning of the packet, while the trail after the packet suggests that another cluster of weaker echo arrivals arrive towards the end of the packet.

Figure 6.12 shows the symbol error rate as a function of the number of coded symbols per sweep, obtained at sea (note that the symbol error rate is on the y-axis, while on the x-axis is the number of coded symbols per sweep). To better distinguish the statistics for S2C packets with a sweep length of 2 ms versus those with a sweep length of 4 ms, different line colors have been used (blue and red,

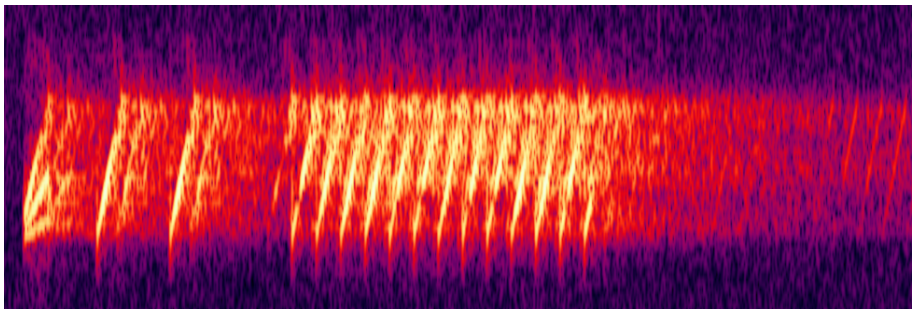

Figure 6.11: Example of received S2C signal at sea.

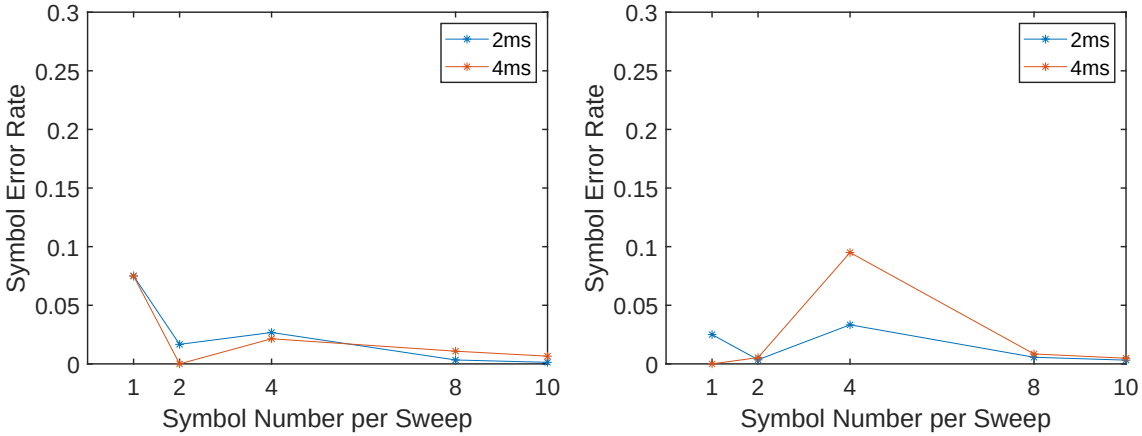

(a) Packet length of 16 sweeps.

(b) Packet length of 32 sweeps.

Figure 6.12: Experiments at sea: symbol error rate as a function of the number of coded symbols per sweep.

respectively). Moreover, since for each configuration ten S2C packets were sent, each point in figure 6.12 represents the average symbol error rate computed over the ten experiments. From the figure, it is clear that the symbol error rate is close to zero for almost all configurations. In some cases, however, the symbol error rate reaches higher values (almost 0.1 in the worst case) and the reason why some particular configurations exhibit such high levels compared to others is still under investigation. Indeed, since such events seem to be isolated cases, it is possible that the channel condition or even the geometry of the experimental environment were not suitable for these particular configurations.

It should be noted that in this paper we mainly aim to present the perfor-

mance and limitations of our S2C implementation in different underwater environments, which to date consists of the basic implementation of the S2C communication method of [8]. Indeed, our implementation considers only the strongest path and neither phase correction or channel estimation, nor the sophisticated receiver presented in [13] are applied at this stage.

Chapter 7

Conclusions

Underwater communications are significantly affected by strong multipath and severe Doppler distortions. In this thesis work, we studied how to correct Doppler effects in JANUS transmissions. In particular, we exploit the JANUS preamble to compute the CAF and compensate Doppler distortions up to 5 ms without requiring any modification to the standard. The effectiveness of our technique has been proven through both realistic simulations and in field experiments. Realistic simulations proved that the proposed method is able to compensate and correctly receive up to 90% of the packets even in the most challenging case of the NCS1 watermark channel and already with a SNR of 2 dB on top of the NOF1 Watermark trace. In field experiments, performed both during the JANUS Interoperability Fest and during the LOON experimental campaign, showed that, with the proposed Doppler estimation, also in real environment and with Doppler distortions up to 5 m/s, a PDR between 97% and 98% can be obtained if a maximum power level is used. While, as expected, a degradation of performance can be observed with a lower level of SNR.

In this thesis work, we also analyze the performance of the S2C modulation based on own custom version of this modulation in MATLAB, where demodulation is accomplished in base band, and only the strongest path is considered. Through extensive simulation and in field experiments, we analyze the impact of different modulation parameters in a variety of channel conditions. The results show that the impact of the bottom depth can be severe and the number of symbols per sweep

should be accurately chosen to avoid reception errors, while Doppler effects can be effectively corrected even at relative speeds of $\pm 5 m/s$. In general, the results reported are good even in shallow waters, as demonstrated by experiments at sea.

List of Publications

[1] C. Baldone, G. E. Galioto, D. Croce, I. Tinnirello, C. Petrioli, "Doppler Estimation and Correction in Underwater Industrial Internet of Things", IMEKO TC-4 International Symposium 2020 - Special session on Wireless technologies, signal processing algorithms and measurement techniques for the Industrial Internet of Things, Palermo, Italy, 2020. DOI: 10.1109/GLOBECOM42002.2020.9348220.

[2] C. Baldone, G. E. Galioto, D. Croce, I. Tinnirello, C. Petrioli, "Doppler Estimation and Correction for JANUS Underwater Communications", GLOBECOM 2020 - 2020 IEEE Global Communications Conference, Taipei, Taiwan, 2020. DOI: 10.1109/GLOBECOM42002.2020.9348220.

[3] C. Baldone, S. Mangione, D. Croce, I. Tinnirello, C. Petrioli, "Performance Analysis of Sweep-Spread Carrier (S2C) Modulation for Underwater Communications". In Proceedings of the 16th International Conference on Underwater Networks and Systems (WUWNet '22), Boston, MA, USA, 2022. Association for Computing Machinery, New York, NY, USA. DOI: 10.1145/3567600.3568147.

Bibliography

[1] Chien-Chi Kao, Yi-Shan Lin, Geng-De Wu, and Chun-Ju Huang. "A Comprehensive Study on the Internet of Underwater Things: Applications, Challenges, and Channel Models". In: *Sensors* 17 (June 2017), p. 1477. DOI: 10.3390/s17071477.

[2] Fausto Ferreira, Roberto Petroccia, and Joao Alves. "Increasing the operational safety of Autonomous Underwater Vehicles using the JANUS communication standard". In: *2018 IEEE/OES Autonomous Underwater Vehicle Workshop (AUV)*. 2018, pp. 1–6. DOI: 10.1109/AUV.2018.8729757.

[3] Milica Stojanovic and James Preisig. "Underwater acoustic communication channels: Propagation models and statistical characterization". In: *IEEE Communications Magazine* 47.1 (2009), pp. 84–89. DOI: 10.1109/MCOM.2009.4752682.

[4] M. Stojanovic, J.A. Catipovic, and J.G. Proakis. "Phase-coherent digital communications for underwater acoustic channels". In: *IEEE Journal of Oceanic Engineering* 19.1 (1994), pp. 100–111. DOI: 10.1109/48.289455.

[5] Stefano Mangione, Giovanni Ettore Galioto, Daniele Croce, Ilenia Tinnirello, and Chiara Petrioli. "A Channel-Aware Adaptive Modem for Underwater Acoustic Communications". In: *IEEE Access* 9 (2021), pp. 76340–76353.

[6] John Potter, Joao Alves, Dale Green, Giovanni Zappa, Ivor Nissen, and Kim McCoy. "The JANUS underwater communications standard". In: *2014 Underwater Communications and Networking (UComms)*. 2014, pp. 1–4. DOI: 10.1109/UComms.2014.7017134.

[7] Paul A. van Walree, François-Xavier Socheleau, Roald Otnes, and Trond Jenserud. "The Watermark Benchmark for Underwater Acoustic Modulation Schemes". In: *IEEE Journal of Oceanic Engineering* 42.4 (2017), pp. 1007–1018. DOI: 10.1109/JOE.2017.2699078.

[8] Konstantin G. Kebkal and Rudolf Bannasch. "Sweep-spread carrier for underwater communication over acoustic channels with strong multipath propagation". In: *The Journal of the Acoustical Society of America* 112.5 (2002), pp. 2043–2052.

[9] Alessandro Biason. *Studio ed elaborazione di dati sulla propagazione acustica sottomarina*. 2012. URL: http://hdl.handle.net/20.500.12608/16137.

[10] Giovanni Ettore Galioto, Domenico Garlisi, Daniele Croce, Leonardo Mistretta, Romina Badalamenti, Ilenia Tinnirello, Costantino Giuseppe Giaconia, Chiara Petrioli, and Petrika Gjanci. "FLUMO: FLexible Underwater MOdem". In: *OCEANS 2019 - Marseille*. 2019, pp. 1–7. DOI: 10.1109/OCEANSE.2019.8867086.

[11] Roberto Petroccia, Gianni Cario, Marco Lupia, Vladimir Djapic, and Chiara Petrioli. "First in-field experiments with a "bilingual" underwater acoustic modem supporting the JANUS standard". In: *OCEANS 2015 - Genova*. 2015, pp. 1–7. DOI: 10.1109/OCEANS-Genova.2015.7271740.

[12] Leonardo Marchetti and Ruggero Reggiannini. "An Efficient Receiver Structure for Sweep-Spread-Carrier Underwater Acoustic Links". In: *IEEE Journal of Oceanic Engineering* 41.2 (2016), pp. 440–449. DOI: 10.1109/JOE.2015.2445251.

[13] K.P. Arunkumar and C. R. Murthy. "Soft Symbol Decoding in Sweep-Spread-Carrier Underwater Acoustic Communications: A Novel Variational Bayesian Algorithm and Its Analysis". In: *IEEE Trans. on Signal Processing* 68 (2020), pp. 2435–2448.

[14] Rudolf Bannasch and Konstantin Kebkal. "Method and devices for transmitting and receiving information". In: (2006). US Patent 6,985,749.

[15] M. B. Porter. *Bellhop Ocean Acoustics Toolbox*. (Online). URL: http://oalib.hlsresearch.com/AcousticsToolbox/.

[16] Michael B. Porter and Homer P. Bucker. "Gaussian beam tracing for computing ocean acoustic fields". In: *The Journal of the Acoustical Society of America* 82.4 (1987), pp. 1349–1359. DOI: 10.1121/1.395269. eprint: https://doi.org/10.1121/1.395269. URL: https://doi.org/10.1121/1.395269.

[17] Michael Porter. "The bellhop manual and user's guide: Preliminary draft". In: (Jan. 2011).

[18] Finn B. Jensen, William A. Kuperman, Michael B. Porter, and Henrik Schmidt. *Computational Ocean Acoustics*. 2nd. Springer Publishing Company, Incorporated, 2011. ISBN: 1441986774.

[19] Paul A. van Walree. ""Channel sounding for acoustic communications : techniques and shallow-water examples" Norwegian Defence Res. Establishment (FFI), Kjeller, Norway, FFI-rapport 2011/00007". In: 2011.

[20] Joao Alves, John Potter, Piero Guerrini, Giovanni Zappa, and Kevin LePage. "The LOON in 2014: Test bed description". In: *2014 Underwater Communications and Networking (UComms)*. 2014, pp. 1–4. DOI: 10.1109/UComms.2014.7017141.

[21] R. Petroccia, G. Zappa, G. Cimino, A. Grati, and J. Alves. CMRE-DA-2021-001. *Environmental data collected on the CMRE LOON tested during the EUMR project: dataset description*. July 2021. URL: https://www.cmre.nato.int/research/publications/technical-reports/data-reports/1638-cmre-da-2021-001.

[22] B.S. Sharif, J. Neasham, O.R. Hinton, and A.E. Adams. "A computationally efficient Doppler compensation system for underwater acoustic communications". In: *IEEE Journal of Oceanic Engineering* 25.1 (2000), pp. 52–61. DOI: 10.1109/48.820736.

[23] Giovanni Zappa, Ivor Nissen, and John Potter. "Doppler compensation for JANUS applied to data collected in the Baltic Sea". In: *4th International Conference and Exhibition on Underwater Acoustic Measurements: Technologies and Results*. June 2011, pp. 20–24.

[24] M. Johnson, L. Freitag, and M. Stojanovic. "Improved Doppler tracking and correction for underwater acoustic communications". In: *1997 IEEE International Conference on Acoustics, Speech, and Signal Processing*. Vol. 1. 1997, 575–578 vol.1. DOI: 10.1109/ICASSP.1997.599703.

[25] Roshen Jacob, Tessamma Thomas, and A. Unnikrishnan. "Fast computation of wide-band ambiguity function and matched filtering in active sonars". In: *2011 International Symposium on Ocean Electronics*. 2011, pp. 40–47. DOI: 10.1109/SYMPOL.2011.6170496.

[26] Joao Alves, Bruno Cardeira, Giovanni Zappa, Fausto Ferreira, Roberto Petroccia, Vincenzo Manzari, Davide Buselli, Petrika Gjanci, Oleksiy Kebkal, Jean-Michel Passerieux, Sabrina Schreiber, Ken Scussel, Carlo Vassale, and Dale Green. "The first JANUS Interoperability Fest - a field report". In: *OCEANS 2019 MTS/IEEE SEATTLE*. 2019, pp. 1–6. DOI: 10.23919/OCEANS40490.2019.8962607.

[27] Sean F. Mason, Christian R. Berger, Shengli Zhou, and Peter Willett. "Detection, Synchronization, and Doppler Scale Estimation with Multicarrier Waveforms in Underwater Acoustic Communication". In: *IEEE Journal on Selected Areas in Communications* 26.9 (2008), pp. 1638–1649. DOI: 10.1109/JSAC.2008.081204.

[28] EvoLogics GmbH. *Underwater Acoustic Modems HS-Series*. (Online). URL: https://evologics.de/acoustic-modem/hs.